Quasi-Isothermal External Short Circuit Tests Applied to Lithium-Ion Cells: Part I. Measurements

Alexander Rheinfeld, [1,*,z] Andreas Noel,[1] Jörn Wilhelm, [1] Akos Kriston,[2] Andreas Pfrang,[2] and Andreas Jossen[1]

[1]*Institute for Electrical Energy Storage Technology, Technical University of Munich, D-80333 Munich, Germany*
[2]*European Commission, Joint Research Centre (JRC), Directorate for Energy, Transport and Climate, Energy Storage Unit, 1755 LE Petten, The Netherlands*

Single-layered pouch-type cells were exposed to quasi-isothermal external short circuit tests to study the influence of electrode loading and tab configuration on the short circuit characteristics. Additionally, test conditions such as initial cell temperature, cell voltage and external short circuit resistance were varied. Keeping the cell's temperature increase below 1°C whilst using a calibrated calorimetric setup, a direct correlation between the electrical and thermal behavior could be shown without occurring exothermal side reactions. Previously studied step-like characteristics in the transient current profile could be confirmed for all cells and test conditions, showing differing durations and magnitudes of the observed plateaus based on ohmic resistances, transport processes and reaction kinetics. Lower electrode loadings, counter-tab configurations homogenizing the current density distribution and higher initial cell temperatures accelerate the short circuit by increasing the cell current due to a reduced effective cell resistance. Whilst the chosen initial cell voltages and external short circuit resistances showed a minor impact on the short circuit dynamics, the initial state of charge revealed a noticeable influence defining the discharged capacity and the amount of generated heat. By post mortem analysis, the observed over-discharge could be correlated to an anodic dissolution of the negative electrode's copper current collector.

Because of their comparably high gravimetric and volumetric energy and power density combined with a high degree of technological maturity and meanwhile low overall cost, lithium-ion batteries are the energy storage solution of choice for multiple of today's applications ranging from mobile devices to electric vehicles and even stationary energy storage solutions. With Li-ion batteries being widely applied in our daily life, reported safety incidents involving this technology have resulted in an increased public attention toward the topic.[1–3] Li-ion battery safety is mainly defined by chemical/toxicological safety and thermal safety. The latter is related to thermal characteristics of the applied materials and chosen architecture which, on the one hand, guarantee a smooth operation of the battery, but, on the other hand, pose a certain risk for a so called thermal runaway if a battery heats up too much.[4–6] Such a heat up, which can exceed the cooling capacity of the battery system, can be either caused by an external misuse of the battery or by an internal fault.[7] In order to guarantee a high level of safety for Li-ion batteries entering the market, a substantial number of regulations and standards has been developed in the past covering mechanical, electrical and environmental or thermal abuse scenarios that may trigger a battery failure.[8]

One of the most common electrical tests is the external short circuit test, which is intended to simulate an accidental connection of the battery terminals.[9–14] For a hard external short circuit, the short circuit resistance is in the same order or lower than the internal high frequency resistance of the battery, resulting in a battery response predominantly affected by its inherent characteristics and not by the test conditions. With increasing battery size and consequently reduced internal high frequency resistance which can easily range below 1 mΩ, a thorough experimental realization of such a truly hard external short is becoming technically difficult.[14] This partly explains why both mechanical and electrical tests provoking a cell-internal short circuit are gaining a lot of attention recently, as such an incident can approach a worst-case scenario for a battery independent of the battery size. Besides the short circuit of the cell, an additional localized heat up is triggered. The combination of a short circuit and a strongly localized

heating can rapidly exceed the onset temperature of thermal decomposition reactions often resulting in a violent failure of the investigated cell. Various triggers for provoking an internal short circuit have been reported in the past ranging from sharp nails [15] and blunt rods[16] to phase change materials[17] and metal pieces[18,19] that need to be elaborately included within the cell during manufacturing. Besides the efforts for designing such a test, the influence of the test parameters on the cell behavior is not quite understood so far which may cause variations in the cell response making an interpretation of reported test data difficult. This becomes especially apparent when looking into the design of e.g. a nail penetration test within which not only the nail's material, surface, diameter, and tip angle can be varied but also the penetration speed, depth, and location of a nail entering a cell may be altered.[8] These test parameters can significantly affect the outcome which has been shown recently for 18650 sized cells in terms of the location and penetration depth of the nail.[20,21] Moreover, the electrical behavior of a battery can mostly not be separated from its thermal behavior, which makes a scientific evaluation of the battery response complicated. Furthermore, the thermal behavior during battery failure is not only dependent on the chemical composition of the active and passive materials used within the cells,[22,23] but also affected by the state of charge (SoC) and state of health (SoH) of the cell and the respective electrodes.[24,25] A dedicated experimental investigation enabling a separation of effects is required for understanding the underlying mechanisms during a short circuit event. This accounts for both internal as well as external short circuits, whereas the focus of this work is laid on the latter in order to study the overall short circuit behavior of a battery in the first place.

Within the first part of this combined work, the experimental basis for a model-based investigation of hard external short circuits is presented which elaborates on a continuation of previously published experimental results.[14] As an enhancement of the external short circuit test, a quasi-isothermal calorimetric setup is presented, which allows a straightforward separation of the electrical and thermal behavior of the investigated single-layered pouch-type cells. Test results of quasi-isothermal external short circuit tests are presented, whereas both the characteristics of the cells itself and the test conditions were altered individually. Following this approach, the influence of (intrinsic) cell specific characteristics and (extrinsic) test conditions on the dynamic response of a battery during external short circuits can be evaluated.

*Electrochemical Society Student Member.
zE-mail: alexander.rheinfeld@tum.de

Table I. Cell and electrode characteristics.

		Negative electrode				Separator	Positive electrode			
		Current collector	Composite electrode				Composite electrode			Current collector
		Copper	Graphite			Polyolefin	NMC-111			Aluminum
	Unit		HP	BA	HE		HP	BA	HE	
Areal capacity[s]	mAh cm^{-2}		1.1	2.2	3.9		1.0	2.0	3.5	
Active material content[s]	wt%		96	96	96		86	86	86	
Binder content[s]	wt%		2	2	2		6	6	6	
Conductive carbon content[s]	wt%		2	2	2		8	8	8	
Gravimetric capacity[s]	mAh g^{-1}		350	350	350		145	145	145	
Thickness[m]	μm	18	39	67	124	25	32	79	141	20

[s]supplier information.
[m]measured with a micrometer screw at three different locations during post mortem analysis.

Experimental

In this section, the investigated cells and chosen short circuit test conditions are presented first. The quasi-isothermal calorimetric setup is described before the calibration and test procedure are characterized. At the end of the section, the carried out qualitative post-mortem analysis is described.

Cells and test conditions.—Within this work, 18 single-layered pouch-type cells were exposed to external short circuit scenarios under quasi-isothermal test conditions. Cells and test conditions were chosen to achieve a most extensive evaluation of both intrinsic cell designs and extrinsic short circuit conditions. The investigated cells were manufactured by Custom Cells Itzehoe GmbH (Germany) comprising graphite anodes and LiNi$_{1/3}$Co$_{1/3}$Mn$_{1/3}$O$_2$ cathodes (NCM-111, in the following written as NMC-111). A mixture of 1 M LiPF$_6$ in ethylene carbonate (EC) : dimethyl carbonate (DMC) 1:1 (by weight) containing 2 wt% vinylene carbonate (VC) was used as electrolyte. The cells varied in terms of electrode loading from approximately 1 mAh cm^{-2}

(i.e. high power loading, HP), 2 mAh cm^{-2} (i.e. balanced loading, BA) up to 3.5 mAh cm^{-2} (i.e. high energy loading, HE) following the overall trend toward higher area specific capacities.[26] Within the specified voltage range of the cell during cycling between 3.0 V and 4.2 V, the NMC cathode was the capacity limiting electrode in order to avoid lithium plating during charging. An overview of the graphite and NMC electrode characteristics for each loading is given in Table I. A summary of the investigated cells and applied test conditions is given in Table II. Besides the targeted electrode loading, the investigated cells varied in terms of the tab configuration. Most cells investigated within this work were configured with wide tabs on opposing sides (i.e. counter-tab design, CT, cells 1 to 14) to optimize the homogeneity of current density distribution along the electrodes. Four of the studied 18 cells were equipped with smaller tabs on the same side (i.e. aligned-tab design, AT, cells 15 to 18) to provoke a more inhomogeneous current density distribution during the short circuit tests compared to the CT cells. Whilst the loading and tab configuration were altered within this study, the width and height of the electrodes of 56 mm × 31 mm was not changed which resulted

Table II. Investigated cells and test conditions.

| Cell specifications			Test conditions					Before test			During test			After test		
No.	Design	C_{th} mAh	T_∞ °C	E_{cell} V	SoC %	Short	t_{rest} h	$C_{4.20V}$ mAh	C_{test} mAh	$R_{1 kHz}$ mΩ	$I_{sc, max}$ A	C-rate	C_{sc} mAh	SoC %	E_{cell} V	$R_{1 kHz}$ mΩ
1[†]	CT	17	25	4.15	96	0 V	15	14.4	13.8	316	9.91	689	16.2	−17	2.12	337
2	CT	17	25	4.15	96	0 V	48	13.6	12.9	306	9.91	730	15.0	−15	2.55	319
3	CT	17	45	4.15	96	0 V	15	13.9	13.3	309	10.59	761	16.2	−20	1.72	524
4	CT	17	55	4.15	96	0 V	15	12.3	11.7	319	10.20	828	14.5	−22	1.47	507
5[†]	CT	35	25	4.15	96	0 V	15	29.7	28.5	328	9.72	327	33.3	−16	2.44	346
6[*†]	CT	35	25	4.15	96	0 V	48	30.1	28.8	338	9.42	313	32.3	−11	2.64	359
7	CT	35	25	4.30	108	0 V	15	29.5	31.9	330	9.26	313	36.5	−16	2.36	522
8	CT	35	25	4.00	82	0 V	15	29.1	23.9	329	9.61	330	27.4	−12	2.64	337
9	CT	35	25	3.85	67	0 V	15	30.0	20.1	321	9.34	310	24.0	−13	2.48	355
10[†]	CT	60	25	4.15	96	0 V	15	60.5	58.1	397	9.01	149	66.2	−13	2.31	430
11	CT	60	25	4.15	96	0 V	48	61.9	59.4	432	8.91	144	67.2	−13	2.52	464
12[*]	CT	60	25	4.15	96	5 mΩ	15	56.6	54.2	470	8.37	148	60.9	−12	2.40	928
13	CT	60	25	4.15	96	50 mΩ	15	60.7	58.7	409	8.33	137	66.6	−13	2.45	472
14	CT	60	25	4.15	96	576 mΩ	15	59.3	57.0	411	5.90	99	63.8	−11	2.63	434
15[†]	AT	17	25	4.15	96	0 V	15	13.8	13.2	293	9.93	719	15.1	−14	2.47	338
16[†]	AT	35	25	4.15	96	0 V	15	33.2	31.9	349	9.59	289	37.0	−15	2.33	367
17[*†]	AT	60	25	4.15	96	0 V	15	56.7	54.3	470	8.55	150	47.9	11	3.49	936
18	AT	60	25	4.15	96	0 V	15	62.4	59.9	470	8.55	137	66.2	−10	2.49	670

[*]Cell showed high-resistance behavior during test.
[†]Cell was opened after test.

in overall nominal capacities of 17 mAh (HP), 35 mAh (BA), and 60 mAh (HE) between 3.0 V and 4.2 V. In accordance with previous work,[14] the influence of cell temperature (cells 1 to 4) and short circuit resistance (cells 10 to 14) was again studied within this work in order to compare the test results to previous results and to study the behavior during solely hard shorts with varying external short circuit resistances. The previous results were obtained from non-isothermal short circuit tests on 10 Ah pouch-type cells and short circuit tests on 4.5 mAh coin cells which were assumed to be isothermal. Within both previous work and the work presented here, cells from the same cell manufacturer were studied. An electrode loading of 2 mAh cm^{-2} was investigated in previous work which is very similar to the here presented BA loading. Furthermore, the influence of initial cell voltage and, hence, SoC was studied (cells 5 to 9). Again, to enable a most straightforward comparison between the test results presented within this study and previous work, the initial cell voltage was set to 4.15 V in most cases.

To sum up, the scope of the chosen cells and test conditions was, on the one hand, to study the influence of inherent cell characteristics such as the electrode loading and tab design and, on the other hand, to evaluate the influence of test conditions such as initial cell temperature, initial cell voltage or SoC and external short circuit resistance.

Experimental setup.—The single-layered electrode configuration of the investigated cells allows for designing a simple, yet quantitative quasi-isothermal calorimetric test. This can help to understand the cell's behavior during excessively high currents beyond its designated operating window by correlating thermal to simultaneously measured electrical signals. Such a test configuration allows to investigate only the main short circuit event, eliminating the effect of exothermal side reactions (e.g. solid electrolyte interphase layer decomposition, reaction of intercalated lithium with electrolyte and fluorinated binder, electrolyte and positive active material decomposition),[4] which can easily dominate the cell behavior at temperatures exceeding 80°C. In order to keep the overall temperature rise of the investigated cells below 1°C (considered quasi-isothermal within this study) without having to apply an active cooling strategy, the cells were placed in-between two copper bars of 45 mm × 45 mm × 90 mm (CW004A, purity 99.9%). To guarantee a good thermal contact between the cell's pouch foil and the two copper bars, thermally conductive (6 W m^{-1} K^{-1}) yet compressible ceramic foils of 0.5 mm thickness (86/600 Softtherm, Kerafol Keramische Folien GmbH, Germany) were used. To reduce the thermal interaction of the setup with the environment, the copper bars were insulated with a 60 mm thick layer of extruded polystyrene foam (XPS, approximately 0.04 W m^{-1} K^{-1}). For measuring the overall temperature rise, Pt100 temperature sensors (accuracy ±0.15°C at 0°C, DIN/IEC Class A) were placed in the center of the copper bars. The Pt100 sensors were attached to the copper bars with a thermal adhesive which also sealed the hole that was necessary to include the sensors. A schematic overview of the experimental setup including the investigated cell designs is shown in Fig. 1. The two Pt100 sensors and another Pt100 sensor attached with Kapton tape to the surface of the positive tab were connected to three individual digital multimeters (34470A, Keysight Technologies Inc., USA). Based on the four-wire temperature measurement and the chosen time-averaging sampling of approximately 1 s per data point, a temperature resolution of ±0.001°C was achieved. In order to reproducibly simulate highly dynamic short circuit conditions, the cells were connected to a single-channel potentiostat including a 10 A/5 V booster in a two-electrode configuration (SP-300, Bio-Logic Science Instruments, France). The entire calorimetric setup excluding the measurement equipment was placed within a custom-built climate chamber which was cooled by Peltier elements and heated with resistive heaters. For the investigated temperatures, the standard deviation of the environmental temperature regulation was ranging below ±0.03°C which was determined with the aid of a reference thermometer (1524, Fluke Corp., USA) equipped with a fast response reference platinum resistance thermometer (5622, Fluke Corp., USA) resulting in a combined accuracy of ±0.015°C to ±0.019°C between
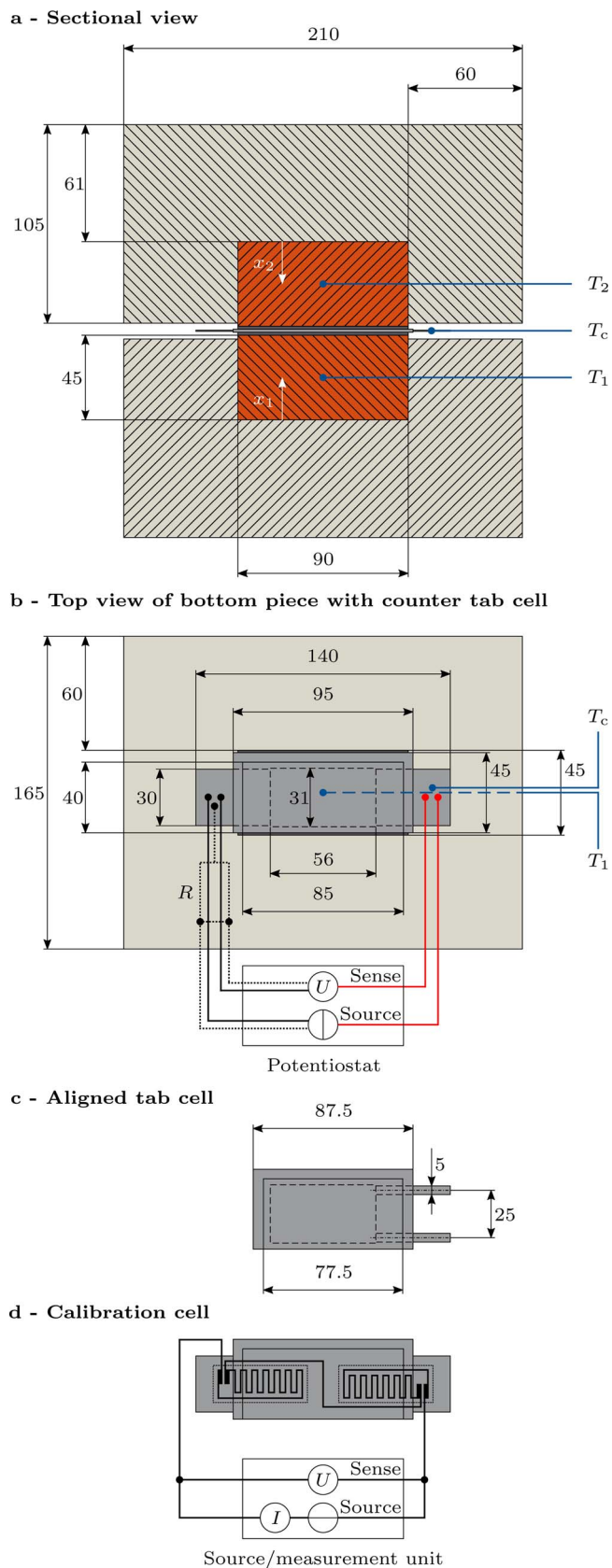
Figure 1. Schematic drawing of the calorimetric setup including a sectional view (a), a top view on the bottom piece of the calorimeter including a representative counter-tab cell (b), a representative aligned-tab cell (c), and a cell used for calibration purposes (d).

Table III. Calibration procedure.

R_{foil} Ω	E_{app} V	I_{app} mA	$\dot{Q}_{\text{app}}$ W	t s	Q_{app} J
1218.4	11.0	9.1	0.1	7200	720
1218.4	34.9	28.6	1.0	720	720
1218.4	78.1	64.1	5.0	144	720
1218.4	110.4	90.6	10.0	72	720

$0°C$ and $100°C$ during the experiments. The measurement equipment was placed outside the climate chamber within the laboratory environment of $25 \pm 2°C$ and was connected to a single desktop computer to allow for a time-synchronization among the used software programs.

Calibration.—Prior to the tests, the measured temperature signal of each Pt100 sensor was corrected by adapting the overall offset and slope of the measurement signal within the considered temperature range toward the reference thermometer. At temperature levels of $25°C, 45°C$, and $55°C$, the calorimetric setup was rested for 24 h within the custom-built climate chamber to allow for a thorough temperature equalization between the sensors and the environment whilst the temperature was simultaneously measured by the three digital multimeters and the reference thermometer. In order to calibrate the calorimetric test setup, i.e to determine the calorimetric constant associated with the overall heat capacity of the setup and losses to the environment, an over-discharged CT dummy cell was equipped with two resistive heater foils. The heater foils were attached on both sides of the cell's surface and were electrically connected in a series configuration. A precision source/measurement unit (B2901A, Keysight Technologies Inc., USA) was used to provide the driving voltage whilst precisely measuring the current so that the generated heat could be calculated (see Fig. 1d). Different voltages were applied to the heater foils, resulting in a heat generation rate of 0.1 W, 1 W, 5 W, and 10 W for a limited amount of time leading to an applied heat of 720 J in each case (see Table III). This value was chosen based on the estimated electrical energy content of the investigated cells ranging from 225 J (HP) to 800 J (HE). The resulting slope of the temperature increment multiplied by the total heat capacitance of the system whilst including losses to the environment represents the applied heat rate. In this configuration (see Figs. 1a, 1b, and 1d), the cell including the attached wiring is considered to be able to exchange heat only with the two copper bars which results in

$$E_{\text{app}} \cdot I_{\text{app}} = C_{p,1} \frac{d\overline{T}_1}{dt} + C_{p,2} \frac{d\overline{T}_2}{dt} + C_{p,c} \frac{d\overline{T}_c}{dt} \qquad [1]$$
$$+ UA_1 \left(\overline{T}_1 - T_\infty \right) + UA_2 \left(\overline{T}_2 - T_\infty \right)$$

where $C_{p,i}$ (J K^{-1}) refers to the total heat capacity, $\overline{T}_i$ (K) to the mean temperature, and UA_i (W K^{-1}) to the overall heat transfer to the environment for each copper bar i. T_∞ represents the environmental temperature. Based on the combined effective heat transfer coefficient U_i (W m^{-2} K^{-1}) and effective heat transfer surface A_i (m^2), UA_i accounts for all heat losses of the calorimeter to the environment including both insulation and wiring. $C_{p,c}$ and $\overline{T}_c$ refer to the total heat capacity and mean temperature of the cell respectively. With the given specific heat capacity $c_{p,\text{Cu}}$ (CW004A: 386 J kg^{-1} K^{-1} at 20°C) and the measured mass m_{Cu} of 1.62 kg for each copper bar, the total heat capacity $C_{p,i}$ is obtained via

$$C_{p,i} = m_{\text{Cu}} \cdot c_{p,\text{Cu}} \qquad (i = 1, 2) \qquad [2]$$

With an average mass m_c of 6.5 g and a specific heat capacity $c_{p,c}$ ranging between 800 J kg^{-1} K^{-1} and 1000 J kg^{-1} K^{-1},[27,28] the total heat capacity of the investigated cells can be estimated analogously via

$$C_{p,c} = m_c \cdot c_{p,c} \qquad [3]$$

The mean copper bar temperature $\overline{T}_i$ and mean cell temperature $\overline{T}_c$ are considered to be represented by the measured temperatures. In order to determine UA_i, the cooling phase after heating up the setup was considered assuming a homogeneous temperature distribution among the components. This assumption allows to separate the individual temperature equalization processes of the two copper bars with the environmental temperature

$$C_{p,i} \frac{d\overline{T}_i}{dt} = UA_i \left(T_\infty - \overline{T}_i \right) \qquad (i = 1, 2) \qquad [4]$$

By introducing the dimensionless temperature Θ_i based on the initial temperature $T_{i,0}$ at the end of the heat-up and the environmental temperature T_∞

$$\Theta_i = \frac{\overline{T}_i - T_\infty}{\overline{T}_{i,0} - T_\infty} \qquad (i = 1, 2) \qquad [5]$$

the solution to this ordinary differential equation can be written as follows[29]

$$\Theta_i = \exp\left(-\frac{UA_i}{C_{p,i}} \cdot t \right) \qquad (i = 1, 2) \qquad [6]$$

which can be individually fitted to the measured exponential temperature decrease and environmental temperature. Knowing each parameter, the theoretical adiabatic temperature $\overline{T}_{\text{ad},i}$ can be determined which is relevant for considering appropriately the generated heat

$$\overline{T}_{\text{ad},i} = \overline{T}_i + \frac{UA_i}{C_{p,i}} \int \left(\overline{T}_i - T_\infty \right) dt \qquad (i = 1, 2) \qquad [7]$$

Including the calculated adiabatic temperature $\overline{T}_{\text{ad},i}$ of the two copper bars in Eq. 1, the effective overall heat capacities of the two copper bars and cell need to be adjusted so that the calculated total heat rate resembles the applied heat rate $\dot{Q}_{\text{app}}$ (W) based on the applied voltage E_{app} (V) and resulting current I_{app} (A)

$$\dot{Q}_{\text{app}} \stackrel{!}{=} \dot{Q}_{\text{tot}} \qquad [8]$$

whereas the total heat rate $\dot{Q}_{\text{tot}}$ calculates as

$$\dot{Q}_{\text{tot}} = \dot{Q}_1 + \dot{Q}_2 + \dot{Q}_c$$
$$= C_{p,1} \frac{d\overline{T}_{\text{ad},1}}{dt} + C_{p,2} \frac{d\overline{T}_{\text{ad},2}}{dt} + C_{p,c} \frac{d\overline{T}_c}{dt} \qquad [9]$$

Allowing for a linear fit of the effective overall heat capacities toward the temperature data, Q_{tot} (J) is further considered here

$$Q_{\text{tot}} = Q_1 + Q_2 + Q_c$$
$$= C_{p,1} \left(\overline{T}_{\text{ad},1} - T_{0,1} \right) + C_{p,2} \left(\overline{T}_{\text{ad},2} - T_{0,2} \right) + C_{p,c} \left(\overline{T}_c - T_{0,c} \right) \qquad [10]$$

with $T_{0,i}$ and $T_{0,c}$ representing the initial temperature of each individual component. By iteratively repeating the steps summarized in Eq. 6, Eq. 7 and Eq. 10 for the applied heat rates, an effective overall heat capacity of 660.7 J K^{-1} for each copper bar and 3.7 J K^{-1} for the cell was determined fulfilling Eq. 8. In the case of the two copper bars, the effective specific heat capacity of 406.5 J kg^{-1} K^{-1} is 5.3% larger than the theoretical value which can be correlated to the influence of the surrounding insulating material, cell wiring and the additional thermal adhesive that was used for attaching the Pt100 sensors. In the case of the pouch cell, an effective specific heat capacity of 562.4 J kg^{-1} K^{-1} can be determined which is lower than the reported data in the literature. This can be explained with the temperature of the tab not fully resembling the mean temperature of the cell based on the location of the Pt100 sensor. With this calibration procedure, the mean error in predicting the applied heat rate can be reduced to as little as 0.1% within the chosen range from 0.1 W to 10 W.

As a measurement setup with a high thermal inertia compared to the specimen was used and local temperatures were measured instead of the mean temperature of the components, an evaluation of this
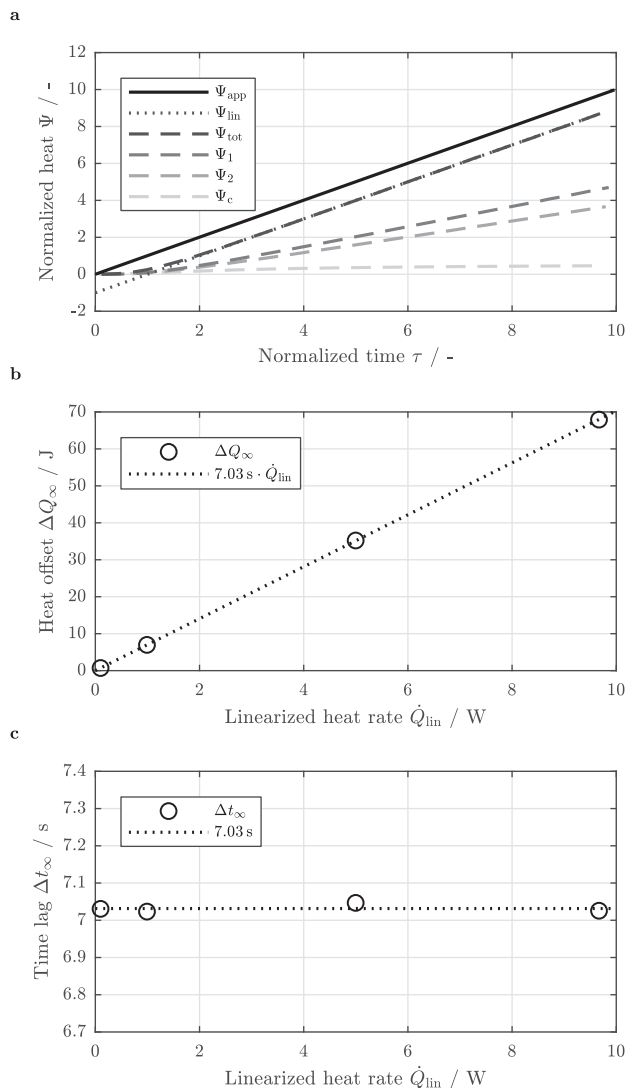
Figure 2. Normalized heat measurement during a calibration procedure at a constant applied heat rate of 10W for 72s (a) and derived absolute measurement error showing the offset in detected heat (b) and the time lag (c) as a function of the linearized measured heat rate ($\tau > 3$). Ψ_j is derived by relating Q_j to ΔQ_∞ (j = app, lin, tot, 1, 2, c).

combined measurement error is needed. Whilst the error accompanied with the positioning of the Pt100 temperature sensors falls below the combined resolution the measurement equipment (see appendix), the measurement error related to the system's thermal inertia cannot be neglected. This *type I thermometer error* is further discussed here.[29] For comparing the carried out calibration tests, the dimensionless heat Ψ and the dimensionless time τ are introduced

$$\Psi = \frac{Q}{\Delta Q_\infty} \qquad [11]$$

$$\tau = \frac{t}{\Delta t_\infty} \qquad [12]$$

which are based on the asymptotic absolute offset in measured heat ΔQ_∞ (J) and the time lag of the measurement Δt_∞ (s). Based on linearizing Q_{tot} as a function of time, both ΔQ_∞ and Δt_∞ can be determined. ΔQ_∞ is represented by the intercept of Q_{lin} with the ordinate and Δt_∞ is defined by the intercept of Q_{lin} with the abscissa. In Fig. 2a, normalized calibration test data is shown for an applied heat rate of 10 W. Due to the normalization procedure following Eq. 11 and Eq. 12, the 5 W, 1 W, and 0.1 W calibration test data look al-

most identical with increasing measurement signal noise at lower heat rates. As shown in this figure, an offset between the predicted and the applied overall heat can be observed. With progressing time, this offset becomes constant. Beyond approximately 3τ, the slope of the predicted heat is also becoming constant allowing for the presented linear fit of the setup's specific heat capacities during calibration. At $\Psi_{lin} = 0$, $\tau = 1$ which resembles the time delay of the measurement. At $\tau = 0$, $\Psi_{lin} = -1$ which represents the offset in the heat measurement. Whilst ΔQ_∞ follows the applied and measured heat rate in a linear fashion (see Fig. 2b), Δt_∞ remains fairly constant around 7s (see Fig. 2c). With

$$\Psi_{app} = \tau \qquad [13]$$

Ψ_{tot} can be further described by the inhomogeneous differential equation

$$\frac{d\Psi_{tot}}{d\tau} + \Psi_{tot} = \tau \qquad [14]$$

which can be solved analytically based on the sum of its particular and homogeneous solution[29]

$$\Psi_{tot}(\tau) = \exp(-\tau) + \tau - 1 \qquad [15]$$

With this solution, the measurement error $\Delta\Psi$ and its derivative $\Delta\dot\Psi$ can be quantified in the course of the measurement

$$\Delta\Psi = \Psi_{app} - \Psi_{tot}$$
$$= 1 - \exp(-\tau) \qquad [16]$$

$$\Delta\dot\Psi = \frac{d\Psi_{app}}{d\tau} - \frac{d\Psi_{tot}}{d\tau}$$
$$= \exp(-\tau) \qquad [17]$$

This allows to derive the errors ΔQ (J) and $\Delta\dot Q$ (W) in measuring the overall heat and heat rate respectively

$$\Delta Q = Q_{app} - Q_{tot}$$
$$= \Delta Q_\infty \left(1 - \exp\left(-\frac{t}{\Delta t_\infty}\right)\right) \qquad [18]$$

$$\Delta\dot Q = \dot Q_{app} - \dot Q_{tot}$$
$$= \frac{\Delta Q_\infty}{\Delta t_\infty} \exp\left(-\frac{t}{\Delta t_\infty}\right) \qquad [19]$$

The short circuit test data Q_{sc} and $\dot Q_{sc}$ presented in this work is corrected based on these findings accordingly

$$Q_{sc} = Q_{tot} + \Delta Q \qquad [20]$$

$$\dot Q_{sc} = \dot Q_{tot} + \Delta\dot Q \qquad [21]$$

whereas t_∞ is considered to be independent of the applied heat rate (7.03s) and Q_∞ is assumed to be directly related to t_∞ and $\dot Q_{tot}$

$$\Delta Q_\infty = \Delta t_\infty \cdot \dot Q_{tot} \qquad [22]$$

as shown in Figs. 2b and 2c.

Short circuit test procedure.—All cells investigated within this study were first cycled outside the calorimetric test setup for 10 cycles at C/2 between the lower and upper cutoff voltage of 3.0 V and 4.2 V using a battery test system (CTS, BaSyTec GmbH, Germany), after which the 1 kHz impedance of the cells was measured at 50% SoC (BT3564, Hioki E.E Corporation, Japan). The discharge capacity of the cells was determined right before the test between 4.2 V and 3.0 V as well as between the upper cutoff voltage of the test (i.e. 4.3 V, 4.15 V, 4.0 V, and 3.85 V) and 3.0 V. For this purpose, a C/2 constant

current (CC) charge and discharge procedure was applied followed by a constant voltage (CV) phase until the current dropped to C/100 at the respective lower and upper cutoff voltage. After the cell voltage or SoC was adjusted according to Table II following a CC/CV charging procedure, the cells were rested for at least 4 h before they were shorted. The cell's discharge capacity between 100% SoC (4.2 V) and 0% SoC (3.0 V) based on the CC/CV procedure was used as the reference for the SoC determination. All tests outside the calorimetric setup were carried out at 25°C within a climate chamber. The main short circuit condition chosen in this work was set to simulate a worst-case scenario, which can be achieved by applying a 0 V CV condition between the working electrode (positive electrode) and the counter/reference electrode (negative electrode) within the used EC-Lab software. The regulation of the 0 V condition was based on a four-wire measurement of the potentiostat. Varying short circuit resistances were simulated as well, whereas the highest resistance chosen in this work (576 mΩ or 1 mΩ m² referred to the electrode area) was applied by using the constant resistance operating mode within the software. Any resistance level below the 1 kHz impedance of the cell caused problems with the stability of the voltage regulation supplied by the potentiostat. Therefore, precision resistors (accuracy ±1%) of 50 mΩ or 0.087 mΩ m² and 5 mΩ or 0.0087 mΩ m² (Power Metal Strip, Vishay Intertechnology Inc., USA) were connected in series to the investigated cells applying the 0 V CV condition (see Fig. 1b dotted lines). Additional resistances due to wiring and electrical contact were ranging below 1 mΩ at 1 kHz. In order to be still able to measure the cell's voltage response during the test, the precision source/measurement unit used for calibrating the calorimetric setup was additionally connected to the cell's tabs (not explicitly shown in Fig. 1b). The short circuit condition was stopped as soon as the current dropped below 0.2 mA or until a control of the potentiostat was no longer possible. This generally resulted in a short circuit duration between 1 h and 3 h depending on the cell behavior. After the short circuit condition was stopped by the potentiostat, the cell remained within the closed calorimetric setup between 15 h and 48 h in order to determine the calorimetric constant for each individual test. A resting time of 48 h before and after the test, both within a closed configuration, was carried out once for each electrode loading in order to determine possible variations throughout the entire test phase. A resting time of 15 h after the test within a closed configuration and an equalization time of 3 h before the test in an opened configuration allowed for performing one test per day without drawbacks in the temperature equalization prior to the short circuit test and in determining the calorimetric constant after the short circuit.

Post mortem analysis.—In order to qualitatively study the impact of the short circuit condition on the investigated cells and electrodes, selected cells were opened in a glove box (M. Braun Inertgas-Systeme GmbH, Germany) under argon atmosphere after short circuit. Punched out electrode samples were washed with DMC and dried subsequently before they were studied by scanning electron microscopy (SEM) and energy-dispersive X-ray spectroscopy (EDX). For this purpose, a benchtop SEM (JCM-6000, JEOL Ltd., Japan) equipped with a MP-00040EDAP detector was used at an acceleration voltage of 15 kV and a working distance of 19-20 mm. EDX mapping was performed at a magnification of 150 and 1000, whereas at the lower magnification the observable area which can be studied by means of the EDX detector is maximized at the chosen working distance (ca. 0.8 mm × 0.6 mm = 0.48 mm²).

Results and Discussion

Within this section, results from the quasi-isothermal short circuit tests are presented and discussed. First, experimental data from an exemplary short circuit test as well as derived calorimetric data is shown. Based on this, the influence of electrode loading, initial cell temperature, initial cell voltage or SoC, short circuit resistance, and tab design is evaluated in terms of absolute values and cell capacity related data. Observed discrepancies in the behavior of certain cells are further correlated to the occurring effective overvoltage and cell resistance.

At the end of the section, selected results from the qualitative post mortem analysis are shown before the underlying mechanisms are discussed leading to the observed behavior which allows for deriving implications in order to design cells and electrodes which may increase a cell's tolerance toward external short circuits.

Short circuit characteristics.—A representative short circuit test is shown in Fig. 3 which was conducted on a HE cell with a CT design (cell 11, see Table II and Figs. 1a and 1b) including a 48 h resting period before and after the test. As can be seen from the voltage data plotted for the entire test duration in Fig. 3a, the applied 0 V condition results in a short circuit duration of approximately 2 h before the test is stopped by the potentiostat and the cell voltage relaxes. Within this condition, the investigated cell delivers a maximum current approaching 9 A (ca. 150C, see Fig. 3b) resulting in a sudden temperature increment of almost 0.6°C of the measured copper bar temperature with respect to the time-averaged environmental temperature ΔT_∞ (Fig. 3c). After the short circuit is interrupted, the cell voltage relaxes above 2.5 V (Fig. 3a) and the temperature of the overall calorimetric setup decreases in an exponential manner (Fig. 3c). Based on this exponential temperature decrease, the unknown parameters of Eq. 6 can be fitted in the same manner as for the calibration procedure. With the aid of these parameters, the heat exchanged with the environment can be determined for the entire setup which is represented by the right term in Eq. 4 for each copper bar. The obtained total heat exchange rate with the environment is shown in Fig. 3g. Looking into the time scales and magnitudes occurring (see Figs. 3b, 3d, and 3f), a logarithmic representation of the short circuit duration and short circuit current is useful.[14] The potentiostat is capable of simulating a worst-case 0 V condition within 50-100 ms for most of the investigated cells (see Fig. 3b). A constant offset of approximately 100 μV toward the electrical ground could be observed for all tests which can be directly correlated to the accuracy of the potentiostat which is 100 μV between 0 V and the maximum voltage of 4.3 V. As has been previously reported,[14] the discharge current reveals a strong step-like behavior within a double-logarithmic representation (see Fig. 3d). Between the initiation of the short circuit and 1s of elapsed short circuit time, a plateau forms at a current level exceeding 8 A (ca. 130C), after which the current drops within a few seconds before a second plateau forms at current values ranging between 1 A (ca. 17C) and 0.1 A (ca. 1.7C). This second plateau lasts from several seconds after the short circuit was triggered up to several hundred seconds before the current drops within a few thousand seconds approaching a third plateau at a current level of 1 mA (ca. C/60) and below. The measured temperature rise shows that both copper bars behave identical throughout the entire short circuit duration. Due to the chosen time averaging sampling condition and the associated resolution of the temperature measurement, a temperature rise below 0.001°C or within 1s cannot be accurately detected with the method presented here, which is why only data is considered beyond this threshold. Whilst there is a continuous rise of the measured temperature up to approximately 1 h, the temperature decreases beyond this point as the generated heat becomes less than the heat transferred to the environment (ca. 25 mW). The measured temperature rise of the positive tab shows a more dynamic behavior of the cell's temperature evolution from the beginning up to approximately 200 s before it follows the temperature of the copper bars (see Fig. 3f). By accounting for the calculated overall heat losses shown in Fig. 3g, the theoretical adiabatic temperature of the test setup can be determined according to Eq. 7. This procedure allows for a determination of the heat generation rate throughout the entire short circuit duration by calculating the slope of the adiabatic temperature rise of the system knowing its total heat capacity as summarized in Eq. 9. By correcting the calculated heat generation rate with the measurement error of the setup as presented in Eq. 21, the true heat rate can be approximated. The result is shown in Fig. 3h, which reveals a very strong resemblance with the measured cell current despite the aforementioned time delay of ca. 7 s which only becomes apparent at early times. The presented correction of the heat signal cannot completely rule out this delay due to the limited
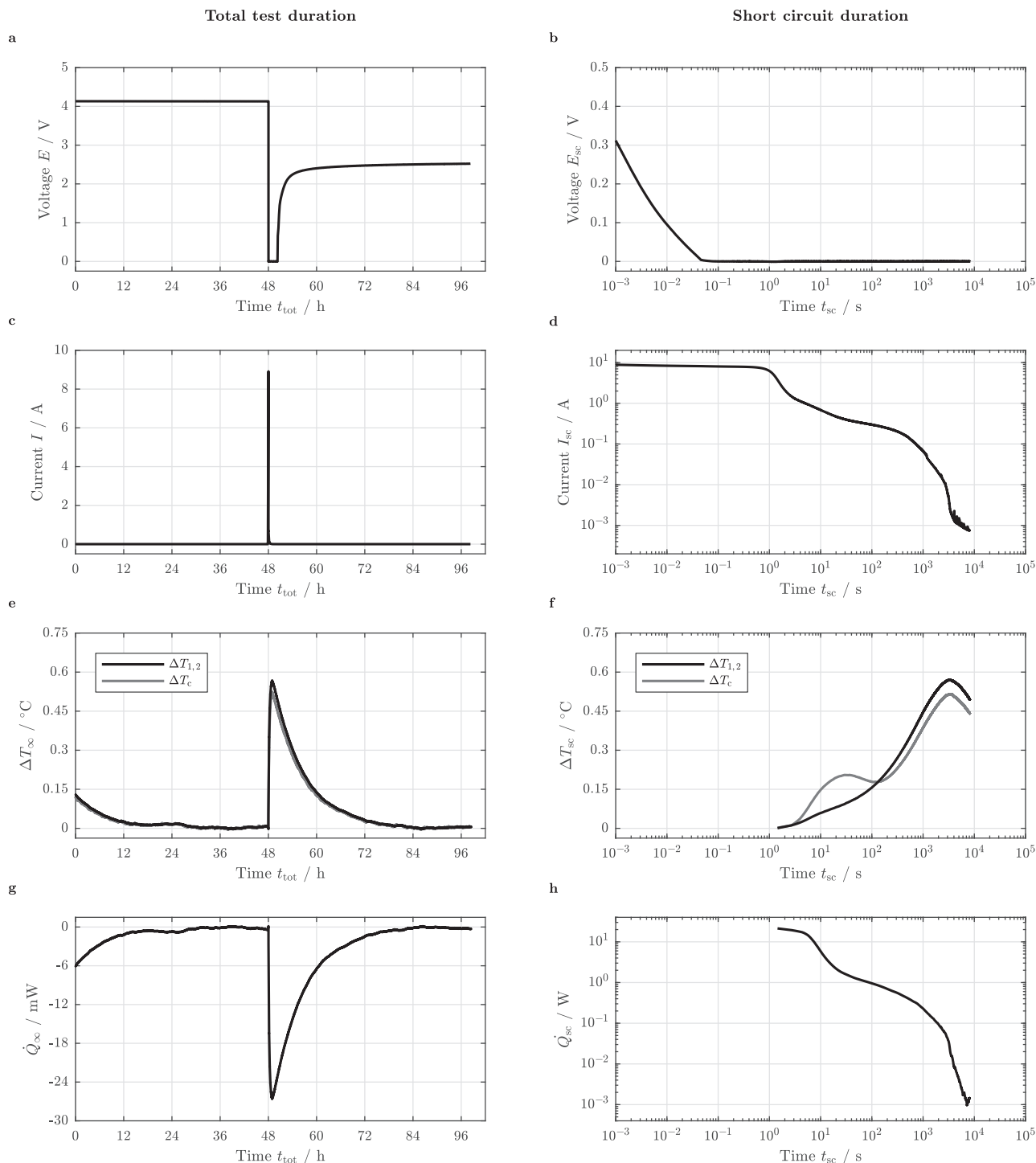
Figure 3. Representative electrical cell behavior (cell 11) during a short circuit test including a 48 h resting period before and after the short circuit event measured with the used potentiostat (a to d) including the thermal behavior measured with the calorimetric setup (e to h) for the entire test duration (left: a, c, e, and g) and the short circuit duration (left: b, d, f, and h).

resolution of the measurement and the unknown heat rate of the cell in the first place. Beyond 21 s ($3\Delta t_\infty$), the heat generation rate can be accurately determined as observed during calibration. The calculated heat generation rate exceeds 10 W in the beginning of the short circuit, forming a similarly shaped plateau between approximately 1 W and 0.1 W before the heat generation rate drops below 1 mW.

By comparing the transient behavior of the investigated cells by both potentiostatic and calorimetric measurements in the following

subsections, similarities and differences between the test results become apparent which can be correlated to the altered cell characteristics and test conditions.

Influence of electrode loading.—In Fig. 4, the short circuit current I_{sc} and time-integrated discharged capacity C_{sc} (mAh) gained from potentiostatic measurements is presented on the left (a, c, and e) whereas the calculated heat generation rate $\dot{Q}_{sc}$ and generated heat
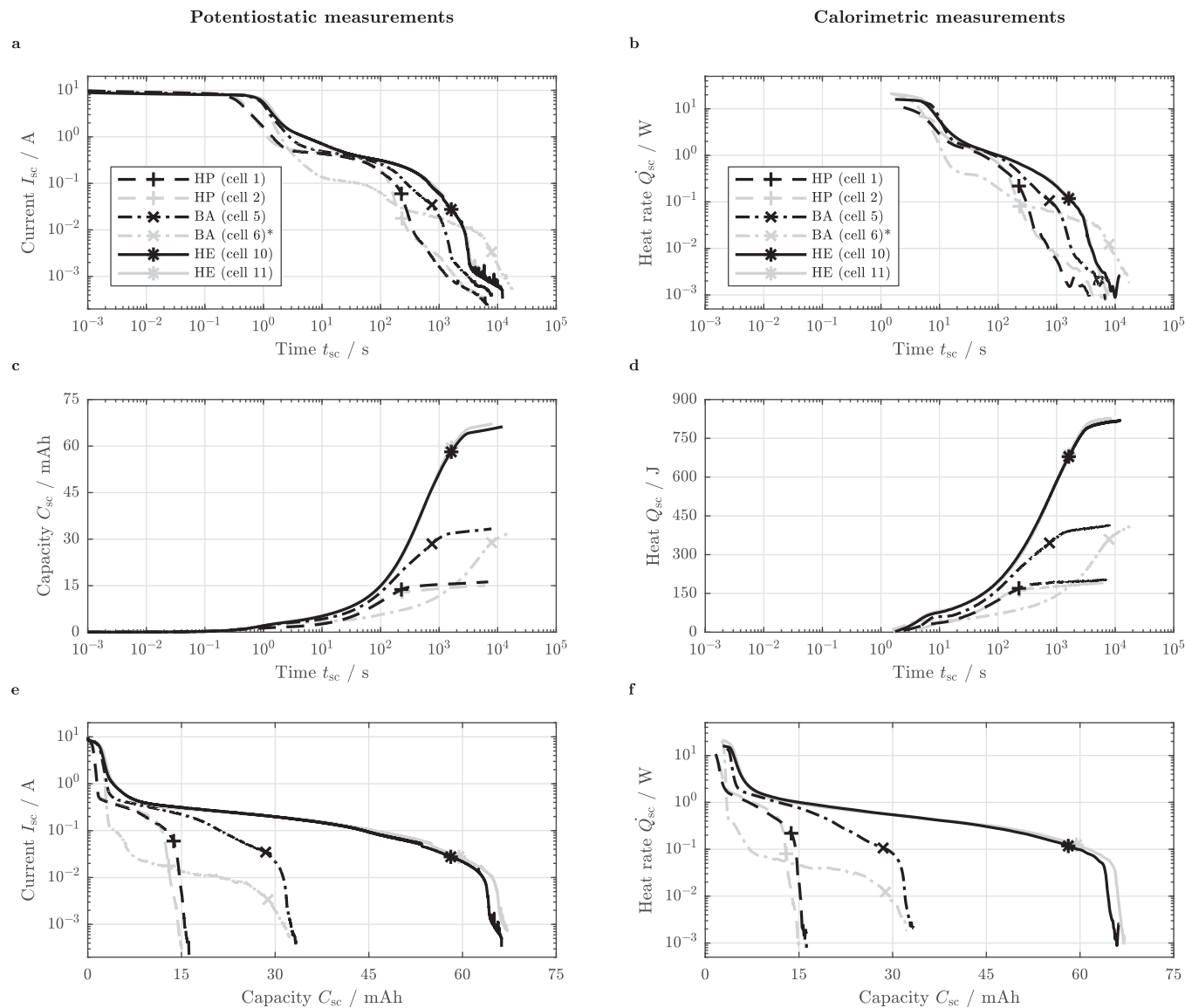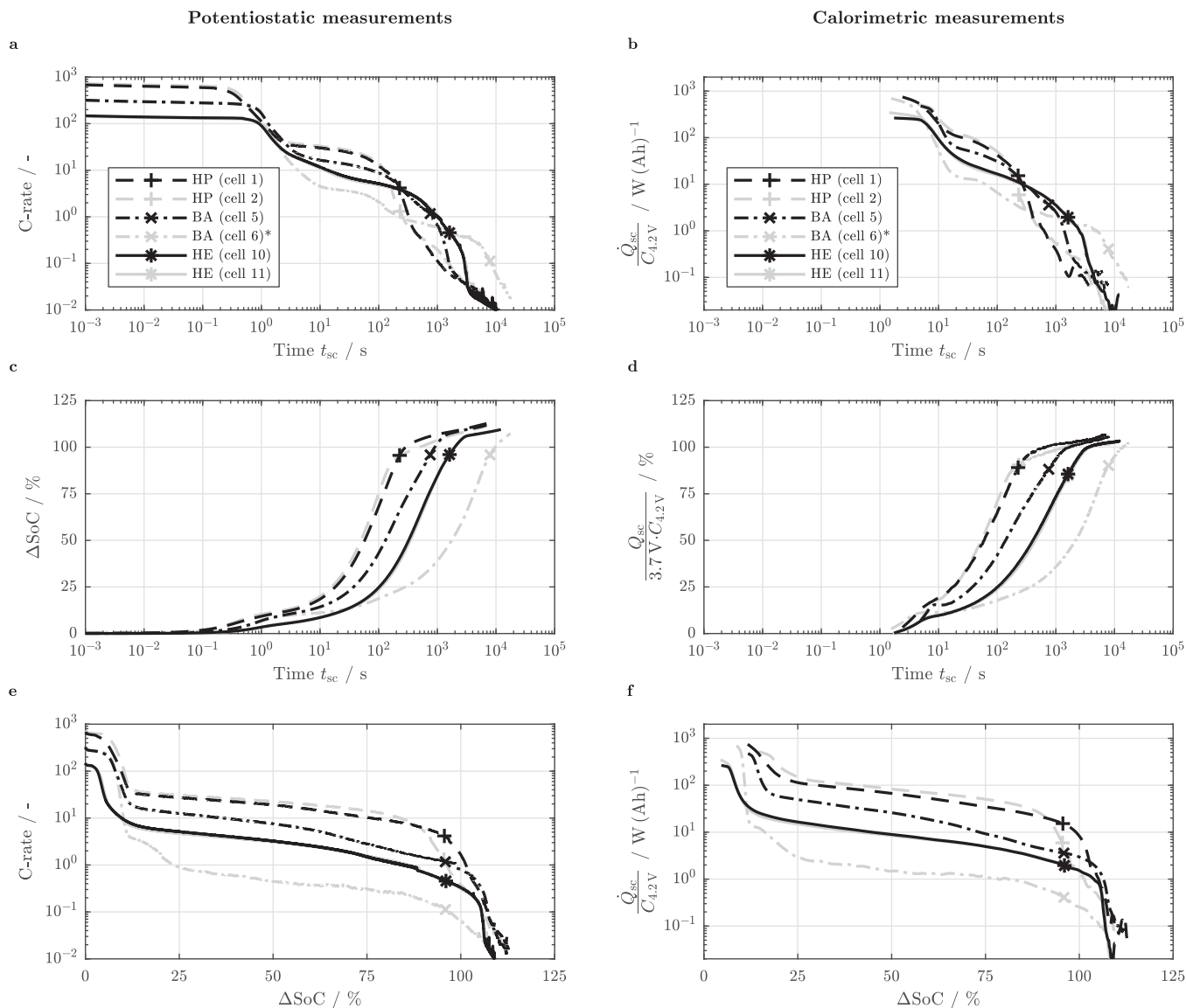
Figure 4. Cell behavior during a 0 V CV short circuit event applied to the HP (dashed lines), BA (dash-dotted lines), and HE loading (solid lines) with a CT design as a function of short circuit duration (a to d) and as a function of discharged capacity (e and f) for the cell current (a and e), heat generation rate (b and f), discharged capacity (c), and generated heat (d) measured with the potentiostat (left: a, c, and e) and the calorimetric setup (right: b, d, and f). Markers indicate 0% SoC. Cell 6 shows a high-resistance behavior (*).

Q_{sc} based on the calorimetric measurements are presented on the right (b, d, and f). All tests were conducted at 25°C applying a 0 V condition to the investigated HP, BA, and HE cells with a CT design (see Table II and Figs. 1a and 1b). As can be seen from Fig. 4, the CT cells investigated in this study generally showed very reproducible characteristics in terms of short circuit current and heat generation rate as a function of short circuit duration t_{sc} (s) (see Figs. 4a and 4b) and discharged capacity (see Figs. 4e and 4f). The strong resemblance between the electrical and thermal behavior of the cells becomes further obvious when comparing the discharged capacity with the total generated heat (see Figs. 4c and 4d). One of the cells shown here comprising a BA loading (cell 6) behaved differently in that respect, which hints at a high-resistance characteristics beyond 1s based on the comparably lower cell current and heat generation rate throughout the second plateau. This will be further discussed in a later part of this section. The peak current $I_{sc, max}$ delivered by the three electrode loadings at the very beginning of the short circuit varies between approximately 9.9 A, 9.6 A and 9.0 A for the HP (cells 1 and 2), BA

(cells 5 and 6), and HE loading (cells 10 and 11) respectively. Previous tests with 18650 cells have shown that a stable control up to 12 A can be achieved with the potentiostat when applying a sudden voltage drop which is sufficient for the investigations made here. The varying peak currents imply that cells with a lower area specific capacity and therefore overall capacity deliver a higher absolute initial short circuit current. Looking into the levels of the 1 kHz impedance measured prior to the tests (310 mΩ, 330 mΩ, and 415 mΩ), a certain correlation to the peak current can be drawn as previously suggested.[30] With increasing the electrode loading in general, both the cell current and the heat generation rate are extended to longer times (see Figs. 4a and 4b). Whilst the current for the HP loading starts dropping toward its second plateau after 0.3 s, both the BA and HE loading take approximately twice as long (i.e. 0.6 s). Furthermore, the HP loading drops below 0.1 A after approximately 200 s, whilst the BA and HE loading can sustain a cell current above this threshold in the range of 300 s and 700 s (see Fig. 4a). This implies that the higher the electrode loading and cell capacity, the longer a certain current level can be sustained, whereas

Figure 5. Cell behavior during a 0 V CV short circuit event applied to the HP (dashed lines), BA (dash-dotted lines), and HE loading (solid lines) with a CT design as a function of short circuit duration (a to d) and as a function of normalized discharged capacity (e and f) for the C-rate (a and e), capacity related heat generation rate (b and f), normalized discharged capacity (c), and electrical energy related heat (d) measured with the potentiostat (left: a, c, and e) and the calorimetric setup (right: b, d, and f). Markers indicate 0% SoC. Cell 6 shows a high-resistance behavior (*).

the overall magnitude of the withdrawn current at each plateau is almost identical, i.e. independent of the cell capacity (see Figs. 4a and 4e). With the heat rate following the cell current, a faster heat up can be observed for cells with a higher electrode loading and overall capacity based on the extended duration of each plateau (see Figs. 4c and 4d). After the cells passed the fully discharged state as defined by the discharged capacity determined prior to the test between the upper cutoff voltage and 3.0 V (indicated via markers in Fig. 4), the cells can still deliver decreasing cell currents and heat generation rates in the same order of magnitude before both drop by one or two magnitudes (see Figs. 4a, 4b, 4e, and 4f). This implies, that fully discharged cells can still contain a considerable amount of electrical and consequently thermal energy. Combined with the thermal stability of the materials and the heat produced based on exothermal side reactions, this may still pose a certain safety risk which, however, is at a comparably low level for the material combination studied in this work.[25]

Relating the current and heat generation rate to the measured capacity between 4.2 V and 3.0 V, a more pronounced difference between

the investigated electrode loadings becomes apparent (see Figs. 5a, 5b, 5e, and 5f). Whilst the HP loading initially provides C-rates beyond 700C, the BA and HE loading fall in the range of 300C and 150C respectively. A spread between the lowest and highest electrode loading up to a magnitude (factor of ca. 5-10) can be observed in terms of C-rate and the adequately capacity related heat generation rate $\dot{Q}_{sc}/C_{4.2\,V}$ (W (Ah)$^{-1}$). In order to be able to better compare the three electrode loadings, an SoC-based representation is useful, whereas the cell is at 100% SoC at 4.2 V and at 0% SoC at 3.0 V following the 0.5C CC/CV procedure.

$$\Delta SoC = \frac{C_{sc}}{C_{4.2\,V}} \qquad [23]$$

As can be seen from Figs. 5e and 5f, the three electrode loadings behave very similarly in terms of the C-rate and capacity related heat generation rate forming plateaus of similar size and shape but varying magnitude throughout the short circuit. All cells are fully depleted at a normalized discharged capacity ΔSoC of approximately 96% which is the discharged capacity of the cells at 4.15 V related to the fully
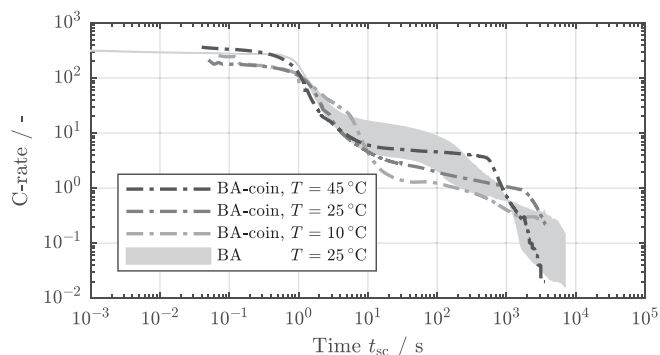
Figure 6. Comparison of cell behavior during a 0 V CV short circuit event applied to coin cells with a similar electrode loading as the BA loading at temperatures of 10°C, 25°C, and 45°C (data taken from Kriston et al.[14] used under CC BY-NC-ND, dash-dotted lines) to the cell behavior of single-layered pouch-type cells with a CT design and a BA loading at 25°C showing varying resistance characteristics (this work, gray shaded area).

charged state at 4.2 V. The first plateau consumes approximately 5% (HE) to 10% (HP) of the cell's capacity within less than a second. The second plateau consumes about 90% (HP) to 100% (HE) of the capacity passing 0% SoC. The third and last 'plateau' which rather resembles a change in curvature in this representation accounts for approximately another 5% (HE) to 15% (HP) of the cell's capacity. The increased magnitude in C-rate from the HE to the HP loading becomes further obvious when looking into the time-integrated normalized discharged capacity (see Fig. 5c). The observed spread in C-rate and capacity related heat generation rate results in a similar shift around a magnitude toward earlier times for the HP loading compared to the HE loading. This implies that the HP cell is fully discharged after just 225 s whilst the BA and HE loading last about 3.4 to 7.2 times as long respectively. This slow down in discharge also decelerates the relative heat up which appears as a shift to the right in Figs. 5c and 5d compared to the HP loading. By relating the generated heat to the cell's electrical energy, the share of thermal energy generated from the electrical energy can be evaluated (see Fig. 5d). With an effective cell voltage around 3.7 V between 100% and 0% SoC, the entire estimated electrical energy of the cell (ca. 3.7 V $\cdot$ $C_{4.2 V}$) is transformed to heat passing the 100% threshold due to the observed over-discharge. This confirms initial approximations for the total electrical and, hence, thermal energy content, as additional exothermal side reactions were suppressed based on the design of the experiment.

Influence of cell temperature.—When looking into previously published data of external short circuit tests on coin cells comprising a similar BA loading[14] and EC:DMC based electrolyte, the temperature has a similar effect on the short circuit behavior of a cell as the electrode loading itself (compare lines in Fig. 6 to Fig. 5a). By increasing the temperature or decreasing the electrode loading, the short circuit is accelerated. This means that both C-rate and capacity related heat generation rate at each plateau are raised toward higher levels resulting in a shorter duration of each plateau, which appears as a shift of the graph toward earlier times. This tendency can be confirmed for cells with a HP loading and a CT design in this work, where the temperature steps were set as 25°C, 45°C, and 55°C whilst applying a 0 V short circuit condition (see Table II). Raising the temperature as high as 55°C was considered to be of more interest in this work than lower temperatures such as 10°C as previously studied,[14] with a short circuit often resulting in a sudden temperature increase beyond the designated maximum operation temperature of the battery under non-isothermal conditions.

When comparing Fig. 7a to Fig. 6, a similar trend can be observed, whereas the impact of the temperature increase is reduced for the single-layered pouch-type cells with a HP loading compared to the coin cells with a BA-like loading. Even though the temperature spread

between the measurements in this work and previous work lies in the same range (i.e. 30°C vs. 35°C[14]), the spread between the plateaus is smaller than previously shown, which especially holds for the second plateau. This could be based on an overall tendency of the coin cells behaving rather resistive in comparison to the investigated single-layered pouch-type cells in this work. This becomes apparent when comparing the coin cell behavior during the second plateau to the observed spread between a pouch-type cell that behaves analogously to other cells investigated in this work (upper boundary of gray area in Fig. 6) to a pouch-type cell that behaves in a high-resistance fashion (lower boundary of gray area in Fig. 6). Similar electrodes and separators were used within both coin cells and pouch-type cells resulting in similar effective transport lengths[31] and accompanied mass and charge transport based overpotentials. However, the assembly process between the coin cells and pouch-type cells is differing resulting in varying compressive forces and consequently diverging contact resistances. This discrepancy might be further increased by the chosen three-electrode configuration of the coin cells.[14]

With increasing the temperature in general, reaction overpotentials are reduced within the electrodes based on Butler-Volmer reaction kinetics increasing the observeable short circuit current. The second plateau being similarly influenced by the electrode loading and temperature further hints at a limitation in mass and charge transport within the liquid electrolyte. With the electrode loading mainly affecting the effective transport length and the temperature affecting the inherent transport properties of the electrolyte itself,[32,33] varying overpotentials are occurring which are based on ion movement. The HP loading being relatively less affected by temperature variations compared to the BA loading might further be a result of the reduced thickness and, hence, superior ion transport compared to the BA loading in the first place (see Table I). Possible mechanisms resulting in the observed characteristics of the short circuit behavior of the cells in each plateau are summarized at the end of the section helping to derive implications toward electrode and cell design. In this study, a further increase in temperature beyond 45°C does not considerably increase the current and heat rate of the short circuit. This becomes especially apparent when looking into Fig. 7c to f. Within the first plateau, the initial C-rate is increased by 9% from 45°C to 55°C which is similar to the increase from 25°C to 45°C (7%). However, the magnitude of the second plateau is not raised much further with respect to C-rate and capacity related heat generation rate beyond 45°C (see Figs. 7e and 7f). As a result, the normalized charge throughput and capacity related heat evolution are not shifted to much earlier times (see Figs. 7c and 7d), implying a certain limitation of the temperature impact.

Influence of cell voltage (state of charge).—As the cell's voltage is the driving force for the current to flow, its influence and consequently the cell's SoC was studied on cells with a BA loading and CT design at 25°C applying a 0 V short circuit condition (see Table II). The initial cell voltage was varied from 4.3 V, 4.15 V, 4.0 V, to 3.85 V resembling an SoC of approximately 108%, 96%, 82%, and 67%. As can be seen from Figs. 8a and 8b, the voltage has a mere influence on the cell's transient behavior up to 100 s to 200 s after the short circuit was triggered. Beyond this point, the higher the voltage and, hence, available cell capacity, the longer a cell can sustain the current level before it drops to the third plateau, which starts after a test duration of 1000 s to 2000 s. Whilst the discharged capacity and generated heat vary for the investigated cells (see Fig. 8c and 8d), the overall duration and magnitude of the first plateau remains almost unchanged. A slight variation in terms of the peak current can be observed, however, this might easily fall within the tolerance of the measurement itself and manufacturing tolerances accompanied with the investigated single-layered pouch-type cells (see Table II).

Referring to the observations made on the influence of electrode loading and temperature, the initial cell voltage or SoC does not affect the dynamics of the short circuit (i.e. the magnitude of current and heat rate) - it defines the overall charge and heat throughput during the short circuit. As the electrode morphology and electrolyte transport

Potentiostatic measurements   Calorimetric measurements
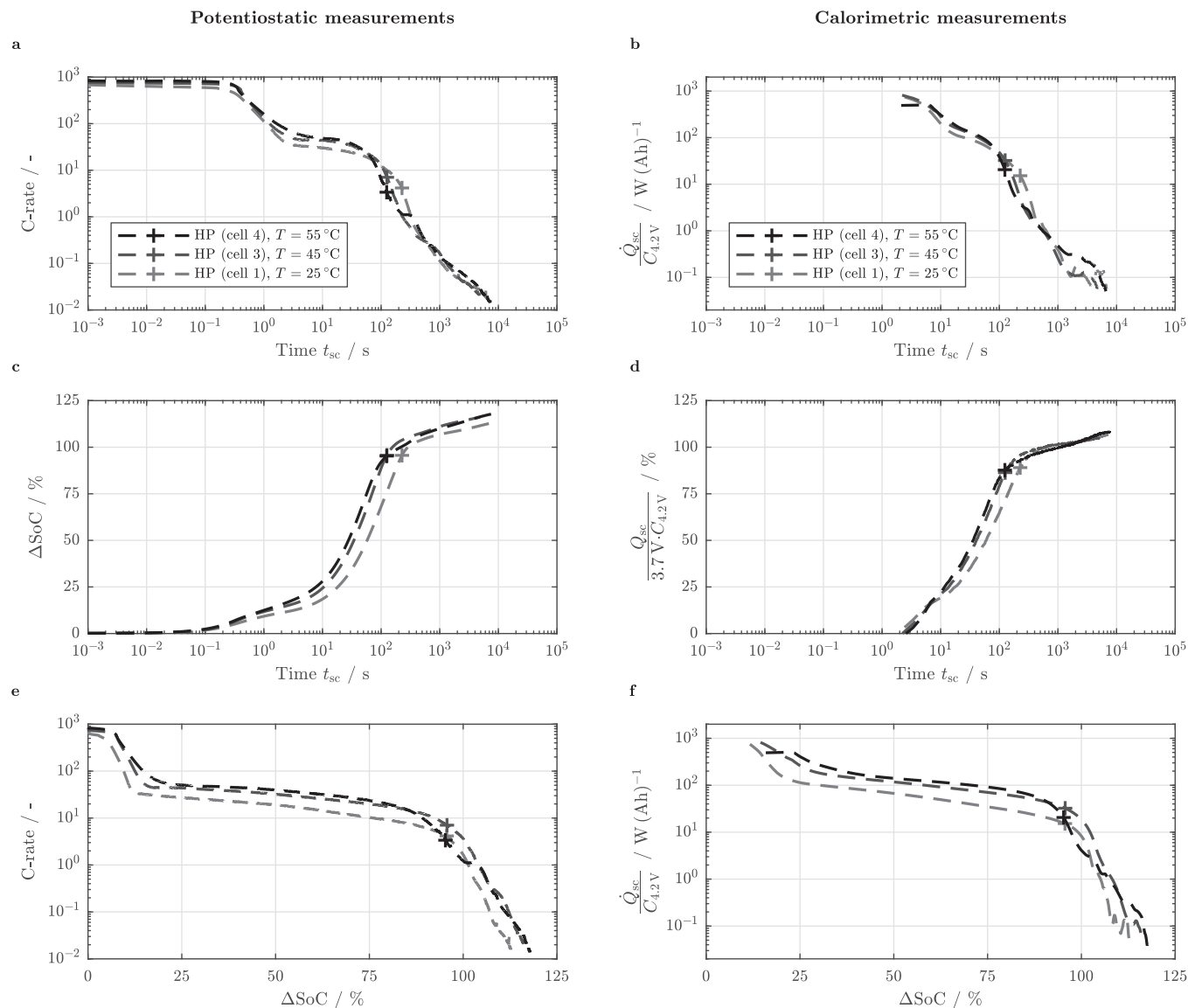
Figure 7. Cell behavior during a 0 V CV short circuit event applied to the HP loading with a CT design at temperatures of 25°C, 45°C, and 55°C as a function of short circuit duration (a to d) and as a function of normalized discharged capacity (e and f) for the C-rate (a and e), capacity related heat generation rate (b and f), normalized discharged capacity (c), and electrical energy related heat (d) measured with the potentiostat (left: a, c, and e) and the calorimetric setup (right: b, d, and f). Markers indicate 0% SoC.

properties are more or less unaffected by the cell's SoC, the magnitude of the second plateau remains unchanged (compare Figs. 8e and 8f to Figs. 5e and 5f and Figs. 7e and 7f). Due to the varying capacity, the second plateau is only changed in its duration. Interestingly, the magnitude of the initial cell current throughout the first plateau is also almost not influenced by the cell voltage which is contrary to previously stated theories.[14,30] Furthermore, the duration of the first plateau is not considerably altered based on the cell's SoC and consequently varying initial degrees of lithiation within the active material particles. Only the slope of the first plateau is marginally changing from the highest to the lowest SoC. Together with the observations made on the influence of electrode loading and cell temperature, each plateau seems to hint at different processes based on the interplay of mass and charge transport as well as reaction kinetics throughout the short circuit. Whilst the first plateau seems to be majorly affected by ohmic resistances throughout the electrodes and the separator and reaction kinetics of the active materials, the second plateau is likely to be dominated by a limited reaction related to ionic resistances espe-

cially in the liquid electrolyte. The influence of ionic resistances based on transport limitations within both solid and liquid phase throughout short circuit scenarios has been studied recently by the Newman group - however, solely based on simulation data.[34] Their work supports these assumptions with a rate limiting influence based on Li-ion depletion of the electrolyte and a simultaneously occurring saturation of the active material particle surface within the cathode during the second plateau increasing charge transfer based resistances. This will be further discussed at the end of the section. When further comparing the evolving C-rate and capacity related heat generation rate as a function of SoC (see Figs. 8g and 8h) to a representation based on the normalized discharged capacity ΔSoC (see Figs. 8e and 8f), the test data shows that cells starting from a lower SoC are even delivering a higher current and heat generation rate in the further process which is possible due to the monotonically decreasing nature of both quantities. This observation supports a theory of consecutively dominating mechanisms limiting the reaction and, hence, current during each plateau throughout the short circuit duration. This could be

Potentiostatic measurements

Calorimetric measurements
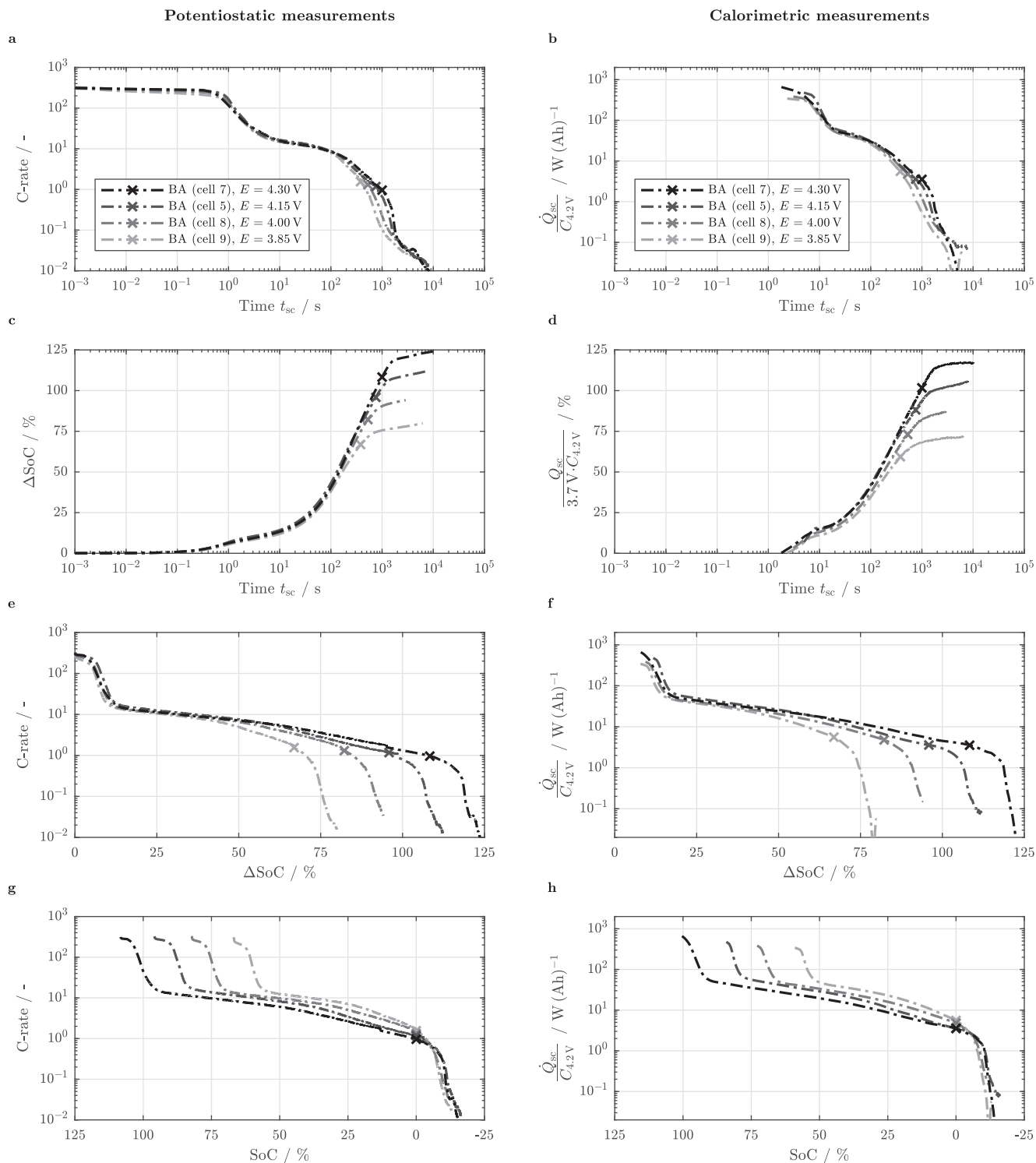
Figure 8. Cell behavior during a 0 V CV short circuit event applied to the BA loading with a CT design at initial cell voltages of 4.3 V, 4.15 V, 4.0 V, and 3.85 V as a function of short circuit duration (a to d), as a function of normalized discharged capacity (e and f), and as a function of SoC (g and h) for the C-rate (a, e, and g), capacity related heat generation rate (b, f, and h), normalized discharged capacity (c), and electrical energy related heat (d) measured with the potentiostat (left: a, c, e, and g) and the calorimetric setup (right: b, d, f, and h). Markers indicate 0% SoC.

e.g. based on the dimensions and morphology of the electrodes and active material particles.

At the end of the short circuit, all cells end up at a similar SoC between −11% and −16%. As the mean cell open circuit voltage as the driving force of the discharge process should be fairly constant throughout the short circuit duration (i.e. between 4.3 V and 3.0 V from 108% SoC to 0% SoC), the effective cell resistance must

vary by orders of magnitude during the short circuit in order to explain the occurring C-rates from as high as 300C to as little as 1C at 0% SoC or C/100 at the end of the short circuit. Hence, it is most likely not the open circuit potential which is dominating the step-like characteristics of the short circuit but the effective resistance of the cell which seems to be mainly related to transport and kinetics related processes and limitations especially with ongoing short circuit
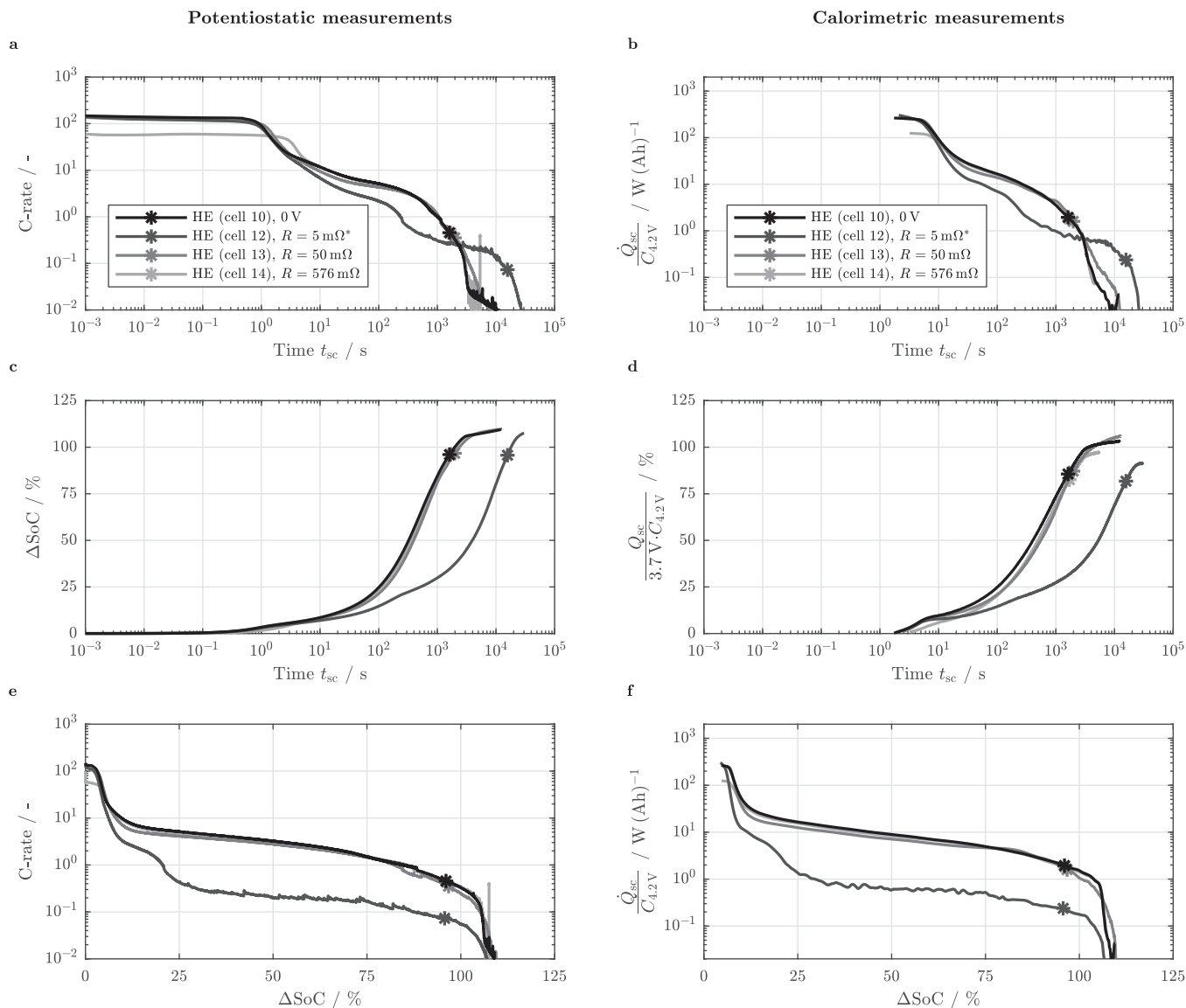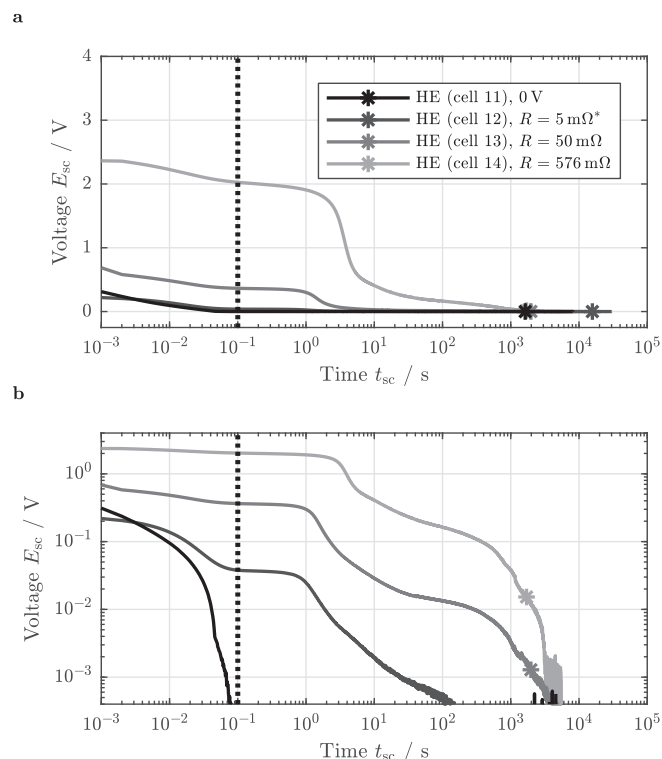
Figure 9. Cell behavior during both 0 V CV and 5 mΩ, 50 mΩ, and 576 mΩ external short circuit resistance events applied to the HE loading with a CT design as a function of short circuit duration (a to d) and as a function of normalized discharged capacity (e and f) for the C-rate (a and e), capacity related heat generation rate (b and f), normalized discharged capacity (c), and electrical energy related heat (d) measured with the potentiostat (left: a, c, and e) and the calorimetric setup (right: b, d and, f). Markers indicate 0% SoC. Cell 12 shows a high-resistance behavior (*).

duration. Instead, what is defined by the initial cell voltage is the overall heat produced in the process according to the available capacity (see Figs. 8c and 8d).

Influence of short circuit resistance.—Besides the open circuit voltage as the driving force and the effective resistance of the cell as the limiting factor for a current to flow, the external short circuit resistance defines the hardness of a short circuit. At 25°C, cells with a HE loading and a CT design were exposed to short circuit resistances ranging from 5 mΩ, 50 mΩ, to 576 mΩ (resistance ratio $R_{sc}/R_{1\,kHz}$ of ca. 0.01, 0.12, and 1.40) and were compared to the most severe short circuit scenario, represented by the 0 V CV condition (see Table II). Weighed with the planar electrode area of the investigated cells, these short circuit resistances represent 0.0087 mΩ m², 0.087 mΩ m² to 1 mΩ m². As an example, a cell with a total electrode area of approximately 0.5 m² resulting in a cell capacity of 10 Ah based on the BA loading,[14] would be correspondingly exposed to a short circuit of approximately 0.02 mΩ, 0.2 mΩ, and 2 mΩ, which would all fall in the classification of a hard external short defined by international

standards and regulations.[8] As shown in Fig. 9, only a minor difference in the transient cell behavior can be identified between cells that behaved normally (i.e. cells 10, 13, and 14). As already observed when comparing cells 5 and 6 of the BA loading, cell 12 which was exposed to the lowest of the chosen external short circuit resistances also showed a high-resistance behavior during the test, whereas an influence of the externally connected precision resistor could be ruled out. Before and after the test, the 1 kHz impedance of each cell with and without the externally connected resistance was measured, which showed no evidence of a variation in the quality of the electrical connection for the investigated cells (i.e. cells 12 and 13). With the measured tab temperature not exceeding a heat up of 1°C, a melting of the contact area as previously observed[14] can be also ruled out. Even though several orders of magnitude of the external short circuit resistance were tested in this work, only the largest external resistance had a noticeably different impact on the cell's behavior, underlining the severity of the other chosen short circuit conditions. Before 5 s of the short circuit have passed, the initial cell current is considerably reduced which can be seen in Fig. 9a. The maximum cell current at

a

b

Figure 10. Cell voltage during both 0 V CV and 5 mΩ, 50 mΩ, and 576 mΩ external short circuit resistance events applied the HE loading with a CT design as a function of short circuit duration in a logarithmic (a) and double-logarithmic representation (b). Markers indicate 0% SoC. Cell 12 shows a high-resistance behavior (*).

the very beginning of the short circuit is 9.01 A, 8.37 A, 8.33 A, and 5.90 A respectively for the 0 V, 5 mΩ, 50 mΩ, and 576 mΩ condition representing 149C, 148C, 137C, and 99C (see Table II). A few seconds after the short circuit was triggered, almost no difference is observable in terms of C-rate, capacity related heat generation rate, discharged capacity and generated heat (see Figs. 9a to 9d). Only an influence on the magnitude of the first plateau can be observed. The second plateau remains almost unchanged (see Figs. 9e and 9f).

When comparing the transient cell voltage as a result of the chosen external short circuit conditions (see Fig. 10), a more pronounced difference between the cells can be observed. After the control of the potentiostat approached a stable voltage level of 100 μV after approximately 100 ms (see vertical dotted line in Fig. 10), the magnitude in varying external resistance values is reflected in the transient voltage response of the cells. Due to the increasing hardness of the short circuit and associated higher initial C-rate with decreasing external short circuit resistance, the first evolving voltage and current plateau is slightly reduced in size (see Fig. 9a and Fig. 10b). Even though the voltage response and consequently overvoltage varies between the different scenarios, the overall cell behavior in terms of charge throughput and generated heat remains almost unchanged, which supports a strongly dominating effective cell resistance during the short circuit event compared to the external short circuit resistance. These observations suggest that an external short circuit resistance in the range of 0.1 mΩ m^2 and below is almost identical to a worst-case 0 V scenario for the investigated HE loading. The intensity of the short circuit especially within the second plateau seems to be independent of the applied short circuit condition, approaching the fully discharged state at more or less the same test duration between 1500 s and 2000 s. Again, the overall heat produced throughout the test is solely dependent on the cell's capacity. With external short circuit resistances above 1 mΩ m^2, a stronger variation in cell behavior has been reported (approximately 2 mΩ m^2, 10 mΩ m^2, 20 mΩ m^2, and 30 mΩ m^2).[14]

Influence of cell design.—In order to evaluate the influence of a more inhomogeneous in-plane current density distribution on the overall cell behavior, cells with slimmer tabs (5 mm vs. 30 mm) aligned on the same side were exposed to a 0 V CV condition at 25°C (see Table II and Fig. 1c). With the electrode loading having the most significant influence on the overall magnitude of the resulting cell current and heat generation rate, again HP, BA, and HE loadings were studied. When comparing the cell behavior of the three electrode loadings between the CT and AT design in terms of absolute current and heat generation rate as a function of normalized discharged capacity (compare Figs. 11a and 11b to 11c and 11d), a stronger variation between the individual electrode loadings can be observed for the AT design (Figs. 11c and 11d). Whilst the HP loading does behave almost identical for both CT and AT designs, the BA and HE loading of the AT design show a stronger tendency toward a high-resistance behavior which means comparably lower currents and heat generation rates throughout the short circuit. Whilst the CT design shows similar values in terms of absolute current and heat generation rate throughout the second plateau for all three electrode loadings (see Figs. 11a and 11b), the AT design shows a variation over a magnitude (see Figs. 11c and 11d). Another indication toward the high-resistance behavior is the duration until the cells are fully discharged. For the AT design, the HP loading is similarly discharged within 160 s (CT: 225 s), whilst the BA and HE loading are approaching the fully discharged state after 1930 s (CT: 760 s) and over 12100 s (CT: 1610 s) which is 2.5 to 7.5 times slower than the CT design. Whilst the behavior of the AT and CT design is similar during the first plateau (i.e. before 1 s of the total short circuit duration), the cell designs vary significantly during the second plateau and the approach of the third plateau (compare Fig. 12 to Fig. 5). The observed difference of more than a magnitude in cell current and heat generation rate between the electrode loadings becomes even more distinct when looking into the C-rate and capacity related heat generation rate of the AT design (see Figs. 12e and 12f). Based on the approximately 100 times lower C-rate and capacity related heat generation rate throughout the second plateau, a stronger time delay between the HE loading compared to the HP loading for the AT design can be observed in terms of normalized discharged capacity and energy released compared to the CT design (see Figs. 12c and 12d as well as Figs. 5c and 5d). With the 1 kHz impedance of the two cell designs being in a similar range, the observed differences are most likely based on the increased inhomogeneity in current density distribution within the electrodes and a resulting larger effective cell resistance. This will be more closely evaluated in the following.

Effective overvoltage and cell resistance.—When relating the generated heat to the discharged capacity Q_{sc}/C_{sc} or referring the heat generation rate to the cell current $\dot{Q}_{sc}/I_{sc}$, an effective overvoltage can be calculated throughout the duration of the test. As an example, this is shown for both cell designs in Figs. 13a to 13d. Ideally, the calculated overvoltage would follow the open circuit voltage of the cell, which is not the case here due to the discussed measurement uncertainties of the calorimetric test setup. With the calorimetric measurement data showing a 7 s time delay, an adjustment period can be observed until the calculated polarization approaches stable values between 4 V and 3 V. This falls in the range below 10% (HE) to 20% ΔSoC (HP) depending on the electrode loading which correlates to more or less 3Δt$_\infty$ (i.e. 21 s, see Fig. 5c). The variation in calculated overvoltage is rather low for time integrated data approaching a fairly constant value of approximately 3.3 V for all electrode loadings which ranges below the nominal cell voltage of 3.7 V (dotted line in Figs. 13a to 13d). The time derivative data shows a slightly higher deviation in the calculated overvoltage exceeding the initial cell voltage of 4.15 V which is physically not meaningful (Figs. 13c and 13d). However, both methods come to similar results throughout most of the short circuit duration with an increasing deviation beyond the fully discharged state based on the limited temperature resolution of the calorimetric test setup and interactions with the environment. The overvoltage again ranges around 3.3 V throughout the entire test duration. By relating the calculated overvoltage to the cell current $\dot{Q}_{sc}/I_{sc}^2$, an effective cell resistance
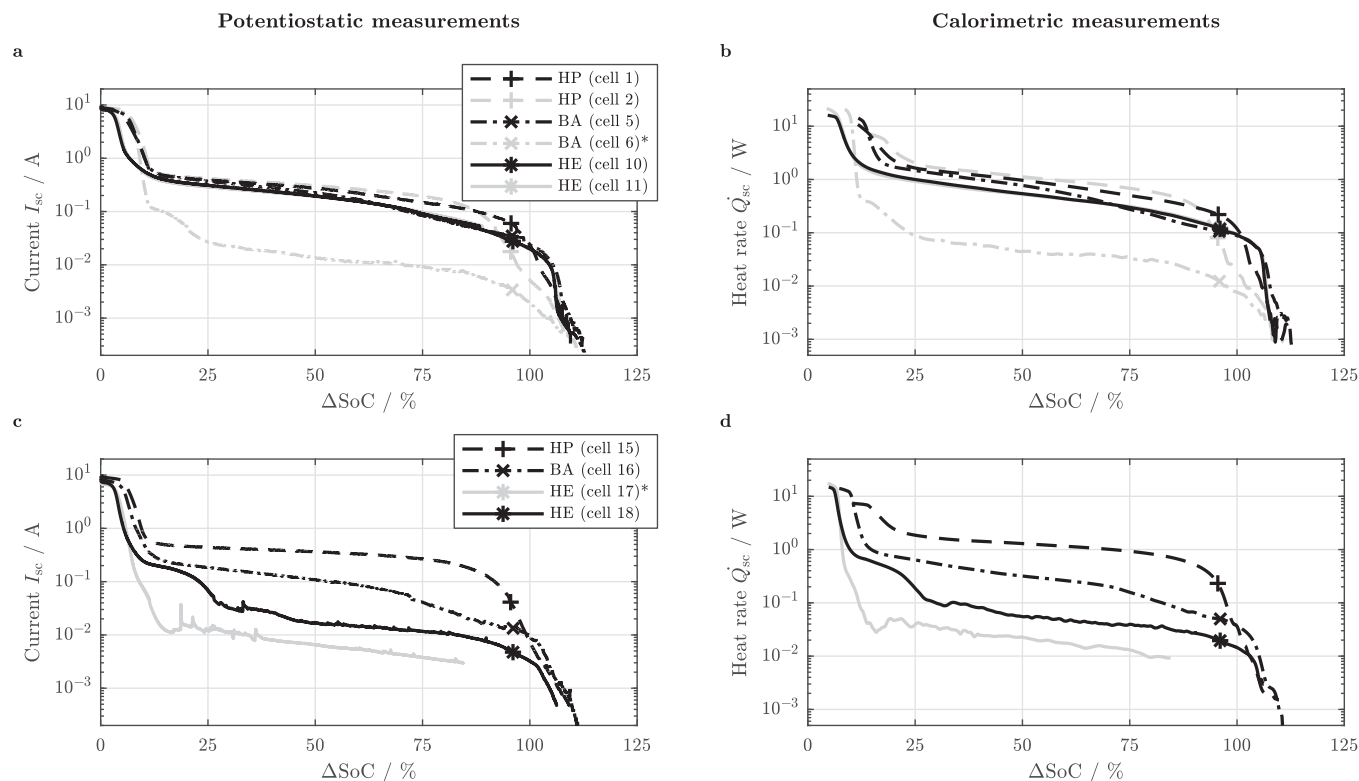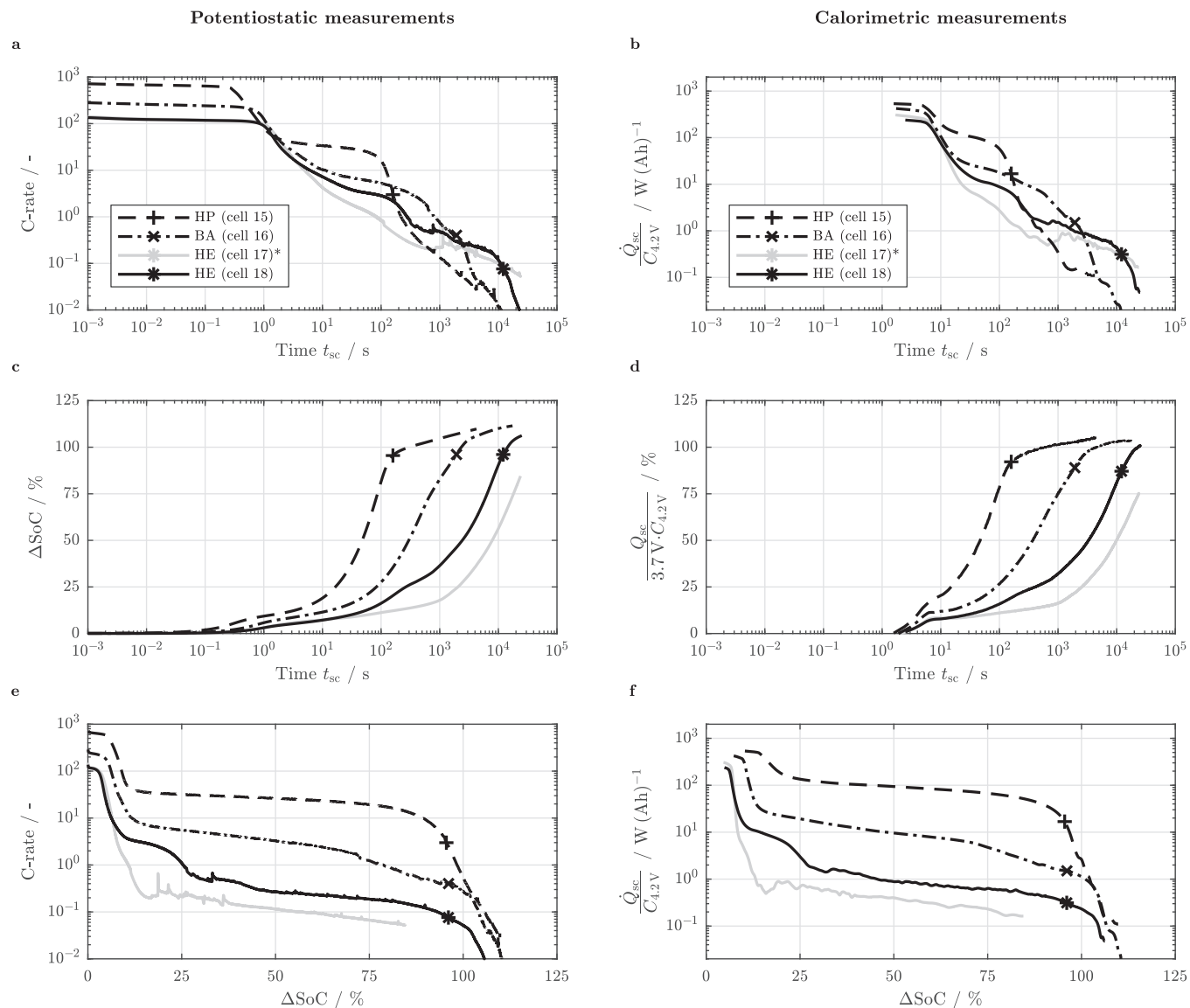
Figure 11. Cell behavior during a 0 V CV short circuit event applied to the HP (dashed lines), BA (dash-dotted lines), and HE loading (solid lines) with a CT (top: a and b) and AT design (bottom: c and d) as a function of normalized discharged capacity for the cell current and heat generation rate measured with the potentiostat (left: a and c) and the calorimetric setup (right: b and d). Markers indicate 0% SoC. Cells 6 and 17 show a high-resistance behavior (*).

can be derived which is shown in Figs. 13e and 13f for the CT and AT design. A considerable increase of the effective cell resistance up to three orders of magnitude can be observed throughout the short circuit duration for both designs (from approximately 10 Ω to 10 kΩ) which underlines the strong transient variability of the effective cell resistance. This observation supports the theory that it is primarily the effective cell resistance which causes the observed strongly varying, step-like characteristics of cell current and heat generation rate throughout the short circuit duration. Within this representation of the cell behavior, also the difference between cells that behave as expected (black lines) and cells that show a high-resistance behavior (gray lines) becomes apparent. All cells that behave unexpectedly, show a resistance increase above 100 Ω after a ΔSoC of just 20%. Furthermore the observed tendency of the AT design showing a higher resistance compared to the CT design especially for the BA and HE loading is also becoming apparent in this representation, with cell 18 of the HE loading bordering the characteristic high-resistance behavior of cells 6, 12 and 17. This means that an increasingly inhomogeneous current density distribution results in a rather restrained short circuit behavior which is very similar to a defective, i.e. highly resistive cell.

Results from post mortem analysis.—During opening the cells after the short circuit tests, visual differences for the electrode loadings and cell designs could be observed. Whilst both the HP and BA loading visually showed no abnormal characteristics for both CT and AT design, copper colored contours could be observed on the cathode surface for cells with a HE loading. Especially cell 10 exhibited distinct copper colored imprints along its middle axis (see upper photograph in Fig. 14a). The exact same contour could be also found on the anode as a black shadow (see mirrored lower photograph in Fig. 14d). Moreover, the anode and cathode coatings with a HP and BA loading were mechanically still well attached to the current collectors. For the HE loading, a poor mechanical integrity of the anode was observed which easily crumbled off the current collector during

handling, especially for the AT design (cell 17). Furthermore, distinct holes of approximately 50-200 μm in diameter were visible across the cathode surface within a fairly homogeneous distance of a few mm between the holes (see Fig. 15). Investigations by both SEM and EDX on the HE electrode samples qualitatively confirmed the occurrence of copper on the cathode surface (see Figs. 14b and 14c) whereas the location of the EDX measurement was chosen at the edge of the copper colored contour (see Fig. 14a). This observation implies local anode potentials exceeding ∼ 3.1 V vs. Li/Li$^+$ in the course of the carried out short circuit test.[35–38] With an open circuit potential around ∼ 1.5 V vs. Li/Li$^+$ in the fully delithiated state, the graphite anode was most likely exposed to an overpotential larger than ∼ 1.6 V below 0% SoC. At a higher magnification, the structure of the copper traces shows to be cauliflower-like and is rather randomly spread across the electrode morphology. Interestingly, traces of copper could be also observed on the anode surface of the investigated HE cells (see Figs. 14c and 14d). These copper traces could have either been transferred to the anode from the cathode during the disassembly process or dissolved copper ions were deposited on the anode surface due to varying anode potentials throughout the short circuit duration. Whether the copper traces were then growing from the anode surface toward the cathode or from the cathode toward the anode remains unclear. The shape and morphology of the deposited copper particle as shown in the center of Fig. 14f, might indicate a growth starting from the anode surface. The detected oxide traces (blue/purple) on the surface of the magnified copper particle most likely resulted from an oxidation process of copper after the sample was transferred from the glove box to the SEM.

In order to better understand the occurrence of copper traces on the cathode surface and the overall cell behavior below 0% SoC, possible scenarios and underlying processes during such an over-discharge are evaluated in the following. Based on a differential voltage analysis of the cells (shown in the second part of this combined work), the electrode balancing between anode and cathode could be stud-
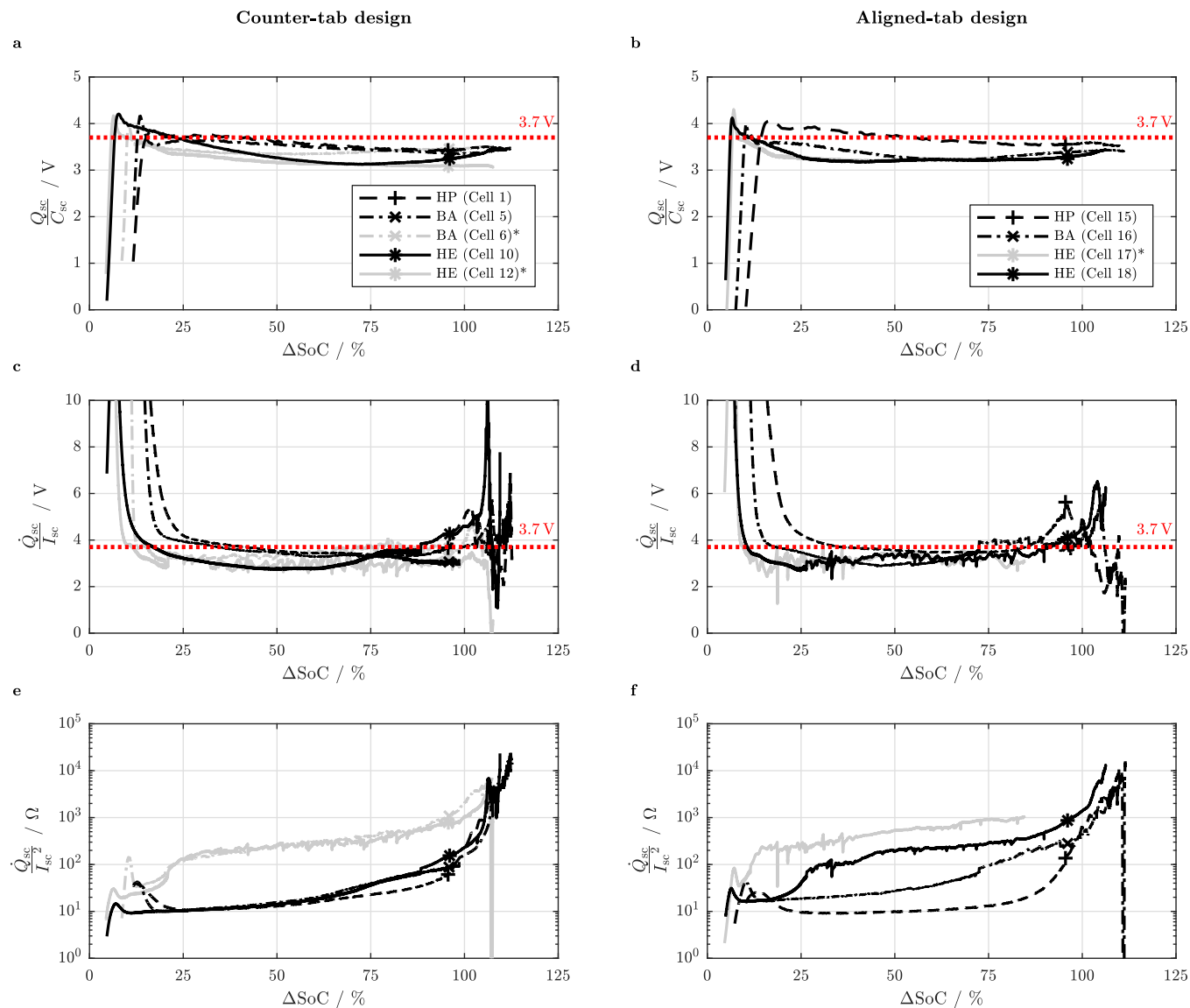
Figure 12. Cell behavior during a 0 V CV short circuit event applied to the HP (dashed lines), BA (dash-dotted lines), and HE loading (solid lines) with an AT design as a function of short circuit time (a to d) and as a function of normalized discharged capacity (e and f) for the C-rate (a and e), capacity related heat generation rate (b and f), normalized discharged capacity (c), and electrical energy related heat (d) measured with the potentiostat (left: a, c, and e) and the calorimetric setup (right: b, d, and f). Markers indicate 0% SoC. Cell 17 shows a high-resistance behavior (*).

ied based on measured (C/50) half-cell and full-cell potentials for each electrode loading prior to the short circuit tests. As more than the 2.4% (HE) to 3.4% (HP) of the capacity left within the anode at 0% SoC could be retrieved from the cells, a different process than a transfer of Li-ions from anode to cathode must have been initiated. With remaining vacancies for Li-ions at 0% cell SoC of 9.4% (HE) to 23.9% (HP) of the cathode's capacity between a cell voltage of 4.2 V and 3.0 V, an ongoing intercalation reaction of Li-ions seems possible. The source for the required Li-ions after the anode is fully depleted, could only be the electrolyte itself. This implies that an additional retrieval of 6.9% (HE) to 20.5% (HP) could be based on a depletion of Li-ions within the electrolyte, whereas the electrons for the intercalation reaction at the cathode surface would be supplied by an anodic dissolution process of Cu at the negative electrode. Based on the rough pore volume within the electrodes and the separator filled with a 1 M LiPF$_6$ based electrolyte, approximately 10% to 15% of the cell's capacity could be retrieved from the electrolyte if the Li-ion concentration was completely depleted. This replacement of solvated Li-ions with Cu-ions would explain the ongoing discharge

process beyond an SoC of −2.4% (HE) to −3.4% (HP). As soon as the cathode reaches its fully lithiated stage or the electrolyte is completely depleted, the only reaction occurring would then be a shuttle reaction of Cu-ions between the anode and cathode. This would fall in the range of the third evolving plateau which was observed especially for the BA and HE loading at currents below 1 mA or 0.1C (see Fig. 4a and Figs. 5a and 5e).

With a molar mass of 63.5 g mol^{-1} of copper and an estimated mass of roughly 280 mg of the copper foil within each cell based on the dimensions of the foil and the density of copper, an additional capacity of approximately 235 mAh could be retrieved from the cells if the whole copper current collector was dissolved into Cu^{2+}-ions and transferred to the cathode. With a capacity between approximately 1.9 mAh (HP) and 5.7 mAh (HE) that were additionally retrieved beyond the depletion of the anode, between 2.3 mg (HP) and 6.8 mg (HE) of copper were dissolved in the process. This implies that almost 3 times more copper must have been involved in the final stage of the short circuit for the HE loading compared to the HP loading. This would explain the observation made that the highest quantity, i.e. the

Figure 13. Calculated effective overpotential (a to d) and effective cell resistance (e and f) during a 0 V short circuit event applied to the HP (dashed lines), BA (dash-dotted lines), and HE loading (solid lines) with a CT (left: a, c and e) and AT design (right: b, d and f) based on the generated heat related to the discharged capacity (a and b) and based on the heat generation rate related to the cell current (c to f). Markers indicate 0% SoC. Cells 6, 12 and 17 show a high-resistance behavior (*).

clearest signal in the EDX measurement, could be observed for the HE loading whilst merely a Cu background noise could be detected for the HP loading.

An explanation for the higher tendency toward a high-resistance behavior of the BA and HE loadings especially for the AT design could be given based on the observed overall increased mechanical degradation of the anode composite electrode and an ongoing cracking of the cathode active material particles even resulting in particles that are split in half (see magnification in Fig. 15c). If the particle cracking on the cathode side is also responsible for the observed holes within the composite electrode is not clear (see Figs. 15a and 15b). Pristine electrodes and both HP and BA loadings gained from cell opening did not show such characteristics.

Discussion of underlying mechanisms and cell design implications.—Based on the experimental results presented in this work, correlations between the design of the investigated electrodes and cells toward a cell's short circuit behavior can be drawn which

may allow for optimizing a cell's tolerance toward abusive short circuit scenarios.

In general, the cell's electrical energy content defines the amount of heat that will be generated throughout a short circuit as long as no additional exothermal side reactions are triggered. This implies that independent of a cell's characteristics toward e.g. delivering a comparably high energy density at predominantly low currents (i.e. high energy) or toward being able to sustain a comparably high power density at predominantly high currents (i.e. high power), only the cell's capacity and its voltage level are relevant for determining the amount of heat that will be produced throughout the short circuit. For a given combination of active materials, the cell's capacity is based on the electrode's active material loading and the size of the electrodes whereas the cell's voltage is defined by the equilibrium potential of both electrodes vs. Li/Li$^+$ which is only marginally affected by the electrode balancing in a given operating voltage range. However, what is altered by a cell's characteristics is the dynamics of the short circuit implying at what rate the cell is discharged and consequently how quickly the stored electrical energy is converted into thermal
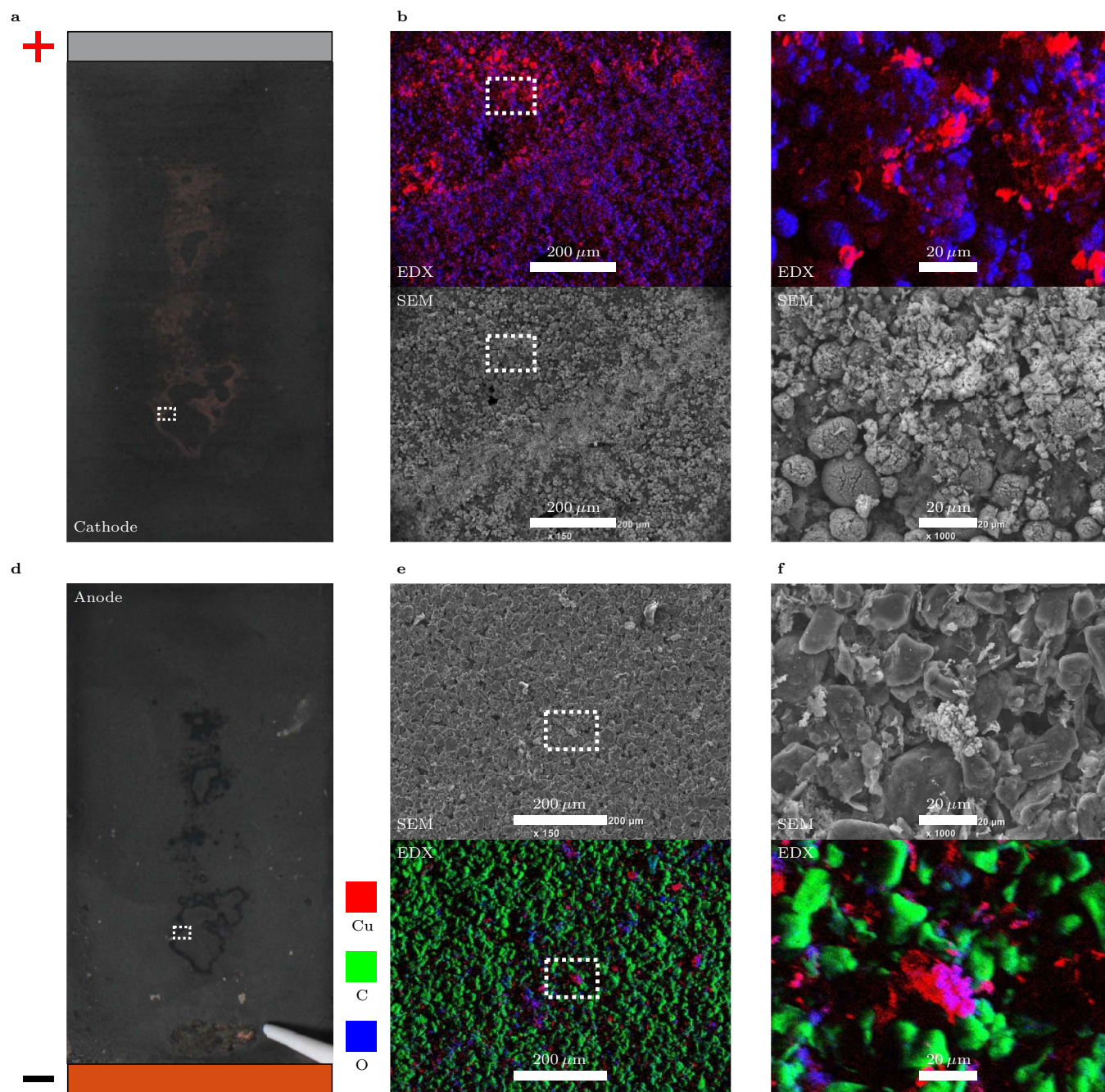
Figure 14. Photographs, SEM images and EDX measurements of both cathode (top: a to c) and anode samples (bottom: d to f) gained from opening cell 10 with a HE loading and a CT design at a magnification of 150 (b and e) and 1000 (c and f).

energy. This can be confirmed when looking into Figs. 4c and 4d and Figs. 5c and 5d. At a constant electrode size, the cell's capacity is only defined by the electrode loading which is over 4 times larger for the highest electrode loading (HE) compared to the lowest (HP) and therefore also generates over 4 times more heat (see Figs. 4c and 4d). With lower electrode loadings generally showing superior rate capability and, hence, power characteristics due to lower cell-internal resistances, the stored capacity and consequently thermal energy is withdrawn around 5-10 times faster for the lowest electrode loading compared to the highest (see Figs. 5c and 5d). In the following, possible mechanisms resulting in the observed short circuit characteristics are evaluated in order to derive implications toward both electrode and cell design.

Three stages of an external short circuit applied to Li-ion cells could be identified which can be characterized by distinct plateaus forming in current and heat generation rate throughout the discharge procedure both as a function of time and discharged capacity. The first plateau consuming around 5–10% ΔSoC within less than a second at currents ranging around 10 A for all electrode loadings and cell designs seems to be majorly affected by ohmic resistances (see $R_{1\,kHz}$ before the test and $I_{sc,\,max}$ during the test in Table II and Figs. 11a to 11d). With the electrodes studied in this work having the same electrode composition (see Table I) showing similar porosities (ca. 45–55%) and all cells comprising the same EC:DMC based electrolyte, the ohmic resistance within both solid and liquid phase scales with the coating thickness which is unaffected by the tab configuration. The
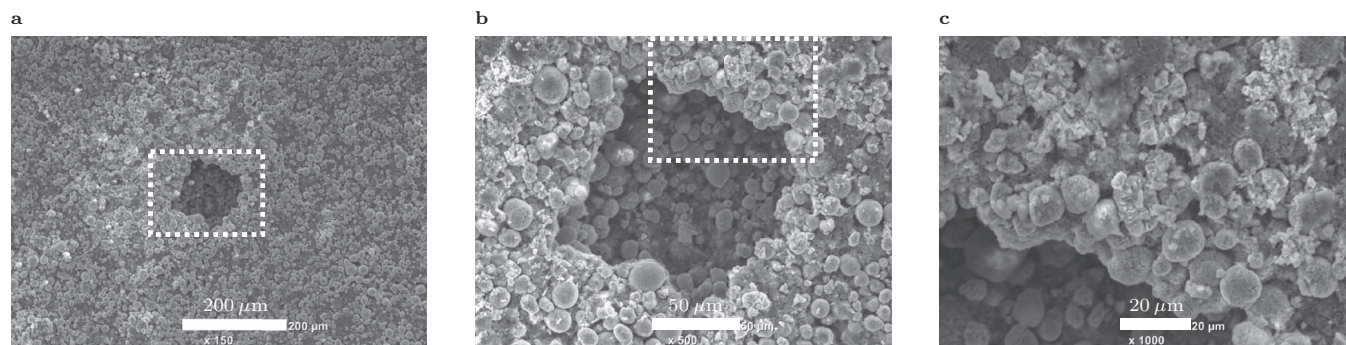
Figure 15. SEM images of a cathode sample gained from opening cell 17 with a HE loading and an AT design showing a representative hole-like structural defect at a magnification of 150 (a), 500 (b), and 1000 (c).

transport length for an electron or an ion to travel is consequently about 3.2 to 4.4 times longer within each electrode for the highest electrode loading compared to the lowest (see Table I) which might explain the considerable difference in initial C-rate between the two (HP: ca. 700C, HE: ca. 150C). With the same active materials used for all cells, the reaction surface area scales with the active material loading of the electrodes. This implies that the lowest electrode loading has a more than 4 times lower active material surface area available for charge transfer reactions occurring within both anode and cathode (see $C_{4.2V}$ in Table II). This circumstance could explain the deviation of the measured initial cell current from the theoretical value based on the open circuit voltage (i.e. 4.15 V) and high frequency resistance of the cells (HP: ca. 310 mΩ, HE: ca. 415 mΩ). Whilst the highest electrode loading delivers approximately 90% of the theoretical maximum short circuit current (E_{cell}/R_{1kHz}), the lowest electrode loading reaches only 74% (see $I_{sc, max}$ in Table II). An increased charge transfer overpotential based on the higher pore-wall flux with decreasing electrode loading might explain this observation.

For the current and heat rate to drop after the first plateau toward the second plateau by over a magnitude (see Figs. 11a to 11d) at a marginally reduced open circuit voltage ($E_{cell} > 4$ V), an additional limitation must be triggered which is differing from a strictly ohmic nature. This process stabilizes for 90–100% ΔSoC over a few hundred seconds (HP) to several thousand seconds (HE). By means of simulation studies, the Newman group has recently shown that beyond 1 s of short circuit duration, a depletion of Li-ions within the electrolyte and a saturation of Li-ions at the surface of the active material particles is likely to occur within the positive electrode.[34] Such a combined scenario would considerably limit the reaction within the positive electrode and would consequently lead to a significantly reduced short circuit current as observed within this study. Furthermore, the impact of electron and ion transport toward the reaction site based on the electrode thickness would again explain the rather constant offset in C-rate and heat generation rate as a function of ΔSoC between the electrode loadings until the cells are fully discharged (see Figs. 5e and 5f). The observed more pronounced decrease in current and heat generation rate with increasing electrode loading for the AT design compared to the CT design is likely to be based on the current density distribution and corresponding stress and strain distribution along the electrodes.[39] Due to a more localized polarization around the 6 times thinner tabs which are furthermore placed right next to each other and not on opposite sides will most likely lead to comparably large currents in the tab vicinity which may result in an overuse of the active material in that area resulting in mechanical degradation of the electrodes (see Fig. 15) and consequently larger ohmic resistances in the further process. This can be confirmed when comparing the effective cell resistance of the CT design to the AT design in Figs. 13e and 13f. Interestingly, the effective cell resistance within the second plateau starts to noticeably increase beyond 50% ΔSoC for all electrode loadings of the CT design indicating a changing nature of the aforementioned reaction limitation (see Fig. 13e) which might be

based e.g. on a dominating solid phase diffusion within the electrodes with decreasing cell SoC instead of an ongoing depletion of the liquid electrolyte. Whilst this is still more or less observable for the HP and BA loading of the AT design, the effective cell resistance of the HE loading is dominated by the increased ohmic contribution.

The third and last plateau forming beyond the fully discharged state (see upper plateau in discharged capacity and generated heat in Figs 4c and 4d) is rather independent of the cell characteristics and plays only a minor role in the short circuit with 5–15% ΔSoC consumed within thousands of seconds at comparably low currents, an open circuit voltage of the cell below 3 V and consequently low heat generation rates. With a fully depleted graphite anode, the ongoing discharge procedure is most likely based on the observed anodic copper dissolution reaction at the negative electrode until the NMC-111 cathode is fully lithiated and/or the electrolyte salt concentration is completely depleted throughout the electrodes.

So, a cell that would be categorized as high power with thin and/or highly porous electrodes and small active material particles resulting in a high specific surface area as well as wide tabs on opposing sides will also result in an accelerated short circuit behavior compared to a cell that is categorized as high energy with thick and/or dense electrodes and large active material particles resulting in a low specific surface area as well as slim tabs on the same side. In order to design a cell which is limiting the external short circuit current and heat generation rate due to its inherent electrode characteristics and tab configuration, a high energy cell with comparably long transport lengths for both electrons and ions combined with a large pore-wall flux at the active material particle surface as well as an inhomogeneous current density distribution along the electrodes might be desirable. Whilst the electrode morphology may also limit the current during an internal short circuit, the tab configuration should only have a minor influence unless a stacked electrode configuration is employed. This implies that by means of the cell design, the duration until a certain amount of heat has been generated during a short circuit can be modified in order to increase the time until a critical temperature threshold is exceeded and/or to reduce the cooling requirements of the thermal management to avoid the occurrence of such critical temperature levels. By further designing a cell with a high energy specific surface area of the cell housing (e.g. small cells) to guarantee limited temperature gradients and a good thermal interaction with the cell's environment, the short circuit current can be further restrained by keeping the cell's temperature as low as possible throughout the process.

However, the short circuit behavior of a cell is clearly not the only design criterion to meet throughout the cell design process resulting in a trade-off between the performance of a cell during normal operation and its tendency toward a self-restrained or unrestrained short circuit characteristics. Furthermore, all implications derived in this work are based on the observation of a complete reaction within both electrodes which is not interrupted e.g. by an evaporation of the electrolyte or by a shut-down mechanism of the separator triggered at elevated temperatures. Based on the geometric size of commercial cells and

limitations of thermal management systems fostering hot-spots within a cell, a premature termination of a short circuit current is likely to occur during external as well as internal short circuit scenarios. Such an event could then either prevent a further heat-up of the cell which would be considered as uncritical or result in further exothermal side reactions dominating the cell behavior which may ultimately result in a hazardous cell failure.

Conclusions

Within this work, 18 single-layered pouch-type graphite/NMC-111 Li-ion cells with varying area specific capacities (HP, BA, and HE) and tab configurations (CT and AT) were short circuited under quasi-isothermal test conditions. Besides the influence of electrode loading and cell design, the impact of cell temperature, initial cell voltage or cell SoC and external short circuit resistance were studied.

A potentiostat was used to apply the short circuit conditions at a constant voltage of 0 V or at varying short circuit resistances. For the purpose of providing a defined quasi-isothermal boundary condition, a calibrated calorimetric test setup was used which allows for an investigation of the heat generation rate whilst the cell temperature is kept almost constant. This test enables a quantitative investigation of the external short circuit behavior alone unaffected by superimposed thermal events such as thermal runaway.

In agreement with previous work, a strong step-like characteristics of the cell current as a function of time and discharged capacity could be observed during external short circuits which was directly reflected by the measured heat generation rate with a time delay related to the measurement setup. Three distinct plateaus in current and heat rate could be observed changing in duration and magnitude based on varying cell characteristics and test conditions. With higher electrode loadings and therefore cell capacities, the electrical and thermal energy released throughout the short circuit is increased which is resembled by a prolonged duration of each plateau in cell current and heat generation rate. The magnitude of each plateau, however is unaffected by the electrode loading for most of the investigated cells (CT). Based on the reduced 1 kHz impedance of the lower electrode loadings, the initial cell short circuit current is even slightly larger for cells with a lower capacity. Relating the measured electrical and thermal signals to the cell's capacity, the smallest electrode loading showed a significantly accelerated short circuit behavior compared to the highest electrode loading, showing larger C-rates resulting in both a faster relative discharge and heat generation rate by a factor up of to 10. Increasing the cell temperature from 25°C to 55°C had a similar effect on the short circuit dynamics as reducing the electrode loading. With increasing temperature, the short circuit is accelerated implying higher cell currents and heat generation rates especially within the first two plateaus. In this work, a temperature increase beyond 45°C did not considerably alter the cell behavior implying a limitation of the temperature influence. With varying initial cell voltages from 4.3 V to 3.85 V and therefore SoC from 108% to 67%, almost no influence on the dynamics of the short circuit could be observed especially within the first plateau. Similar to the electrode loading, the overall capacity defines the amount of generated heat which can be correlated to the duration of the second plateau. It could be observed that both transient current and heat generation rate are strongly depending on the amount of charge withdrawn from the cell almost unaffected by the SoC until a cell approaches the fully discharged state. This implies that for a lower initial SoC, larger currents and heat generation rates can be measured as a function of SoC compared to a cell shorted at a higher initial SoC. The magnitude of the external short circuit resistances ranging from about 0.01 mΩ m^2 to 1 mΩ m^2, influenced the cell behavior during the first plateau, i.e. within the first few seconds. Beyond that, almost no difference could be observed between the cells. Short circuit resistances below 0.1 mΩ m^2 resemble a worst-case 0 V CV scenario. With slim tabs aligned on the same side of the electrodes (AT) compared to wide tabs on opposing sides (CT), the inhomogeneity of in-plane current density distribution is increased. As a result, the C-rate and capacity related heat generation rate are reduced by a factor up to

100 for the highest compared to the lowest electrode loading. This spread is about 10 times larger than observed for a homogeneous current density distribution. When comparing the calculated overvoltage and effective cell resistance for the two cell designs, a fairly constant overvoltage around 3.3 V can be observed, whereas the effective cell resistance rises from approximately 10 Ω to 10 kΩ with ongoing short circuit duration. Cells that behaved abnormally showing comparably lower cell currents and heat generation rates also revealed a more than 10 times larger effective cell resistance. With increasing inhomogeneity of the current density distribution, a higher tendency toward such a high-resistance behavior can be observed especially for higher electrode loadings. As part of a qualitative post mortem analysis, selected cells were opened and studied visually and by means of SEM and EDX. With an ongoing discharge of the cells beyond up to −20% SoC, a continued intercalation of the cathode active material particles and simultaneously occurring anodic copper dissolution is likely. Traces of copper could be qualitatively confirmed via EDX on both the cathode's and anode's surface especially for the highest electrode loading. The observed increased tendency for the occurrence of copper on the electrode surface with increasing electrode loading may be correlated to the amount of charge transferred between the two electrodes beyond the fully discharged state. The increased tendency toward a high-resistance behavior for higher electrode loadings might be based on the reduced mechanical integrity of the anode and the observed severe mechanical degradation of the cathode which seems to be triggered by an inhomogeneous current density distribution.

Due to the more self-restrained short circuit behavior, cells with a high energy characteristics comprising thick and/or dense electrodes, large active material particles and thin tabs placed next to each other are favorable compared to high power cells with thin and/or highly porous electrodes, small active material particles and wide tabs on opposite sides. Possible underlying mechanisms were discussed pointing out the significance of ohmic losses and charge transfer overpotentials within the first plateau, limited ion diffusion involving a depletion of Li-ions in the liquid electroylte accompanied by a saturation of Li-ions at the surface of the active material particles within the positive electrode during the second plateau and an ongoing intercalation reaction of the positive electrode based on an anodic copper dissolution reaction throughout the third plateau.

Further experimental work will focus on the comparison of external with internal short circuit conditions within the same calorimetric setup in order to evaluate the impact of the locality of a short circuit on its severity.

In the second forthcoming part of this combined work, the underlying mechanisms for the observed dynamics of the external short circuit behavior will be studied by means of a validated physical-chemical model.

Appendix

As the temperature within the center of the copper bars was measured instead of the mean copper bar temperature, an evaluation of this error is necessary. Based on the measurement setup including a thermal insulation of all components, the setup is exchanging only a small amount of heat with the environment. This allows for the assumption of no-flux or symmetry boundary conditions at the interface between each copper bar and the surrounding insulating material resulting in a one-dimensional heat conduction problem. Introducing the spatial coordinate x_i (m) along the normal direction of the cell's surface
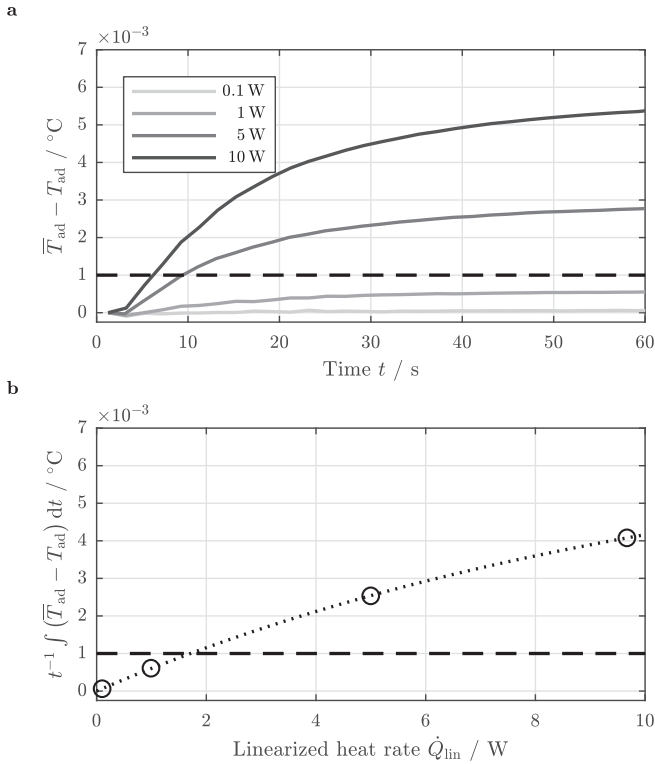
Figure A1. Measurement error accompanied with the placement of the temperature sensors as a function of time (a) and as a function of measured heat rate (b). The dashed line indicates the resolution of the measurement equipment around $\pm 0.001°C$.

(see Fig. 1a), the partial differential equation of this problem can be written as follows

$$\frac{\partial T_i}{\partial t} = a \frac{\partial^2 T_i}{\partial x_i^2} \qquad (i = 1, 2) \qquad [A1]$$

with T_i representing the spatio-temporal temperature within each copper bar and a ($m^2\,s^{-1}$) representing the thermal diffusivity of the material

$$a = \frac{k_{Cu}}{\rho_{Cu} \cdot c_{p,\,Cu}} \qquad [A2]$$

In Eq. A2, k_{Cu} ($W\,m^{-1}\,K^{-1}$) represents the thermal conductivity (CW004A: 394 $W\,m^{-1}\,K^{-1}$ at 20°C) and ρ_{Cu} ($kg\,m^{-3}$) the density of copper (CW004A: 8930 $kg\,m^{-3}$ at 20°C). In order to solve Eq. A1 analytically, the dimensionless coordinate ξ_i is introduced by normalizing x_i with the thickness X of the copper bars (i.e. 45 mm, see Fig. 1a)

$$\xi_i = \frac{x_i}{X} \qquad (i = 1, 2) \qquad [A3]$$

Furthermore, the dimensionless spatio-temporal temperature Θ_i^* is introduced

$$\Theta_i^* = \frac{T_i - T_{0,i}}{T_{\text{ref},i}} \qquad \forall \xi_i \in [0; 1] \qquad (i = 1, 2) \qquad [A4]$$

whereas $T_{0,i}$ is the initial, homogeneous temperature of each copper bar. Based on the chosen calibration procedure, a constant heat flux $\dot{q}_i$ ($W\,m^{-2}$) from the cell to each copper bar can be assumed. In this specific case, the constant reference temperature $T_{\text{ref},i}$ can be defined as

$$T_{\text{ref},i} = \frac{\dot{q}_i \cdot X}{k_{Cu}} \qquad (i = 1, 2) \qquad [A5]$$

Together with the Fourier number

$$\text{Fo} = \frac{a \cdot t}{X^2} \qquad [A6]$$

the partial differential equation in Eq. A1 can be rewritten in its dimensionless form

$$\frac{\partial \Theta_i^* (\text{Fo}, \xi_i)}{\partial \text{Fo}} = \frac{\partial^2 \Theta_i^* (\text{Fo}, \xi_i)}{\partial \xi_i^2} \qquad (i = 1, 2) \qquad [A7]$$

Based on the particular and homogeneous solution of this dimensionless partial differential equation, the general solution for the problem can be derived[29]

$$\Theta_i^* (\text{Fo}, \xi_i) = \left(\frac{\xi_i^2}{2} + \text{Fo} \right) - \left(\frac{1}{6} + \sum_{k=1}^{\infty} \frac{2 \cos \delta_k}{\delta_k^2} \cos (\delta_k \xi_i) \exp \left(-\delta_k^2 \text{Fo} \right) \right) \qquad (i = 1, 2)$$

$$[A8]$$

with δ_k representing the eigenvalues of the Fourier series

$$\delta_k = k\pi \qquad [A9]$$

approximated with k ranging from 1 and 100. Knowing the transient temperature T_i and the initial temperature $T_{0,i}$ at the center of each copper bar (i.e. $\xi_i = 0.5$), $T_{\text{ref},i}$ and consequently q_i can be estimated. Based on this estimation, the difference between the mean temperature and the measured temperature can be evaluated via a spatial integration of the above equation within 0 and 1, resulting in

$$\overline{\Theta}_i^* (\text{Fo}) = \text{Fo} - \sum_{k=1}^{\infty} \frac{2 \cos \delta_k \sin \delta_k}{\delta_k^3} \exp \left(-\delta_k^2 \text{Fo} \right) \qquad (i = 1, 2) \qquad [A10]$$

which allows to calculate $\overline{T}_i$ following Eq. A4 and consequently the measurement error in predicting the mean adiabatic temperature following Eq. 7

$$\overline{T}_{\text{ad}} - T_{\text{ad}} = \frac{\overline{T}_{\text{ad},1} - T_{\text{ad},1}}{2} + \frac{\overline{T}_{\text{ad},2} - T_{\text{ad},2}}{2} \qquad [A11]$$

The calculated error is shown in Fig. A1 as a function of time for the applied heat rates (a) and as a of function heat rate for the time-averaged error (b). With measured total heat rates below 5 W after 10 s even for the HE loading (see Fig. 3h), and an average heat rate around 0.1 W and below throughout the duration of the short circuit, the measurement error falls below the accuracy of the measurement equipment (dashed line in Figs. A1a and A1b) and can be therefore neglected.

ORCID

Alexander Rheinfeld https://orcid.org/0000-0003-0995-7266
Jörn Wilhelm https://orcid.org/0000-0002-5649-2580

References

1. Samsung, [Infographic] Galaxy Note7: What We Discovered. 2017; https://news.samsung.com/global/infographic-galaxy-note-what-we-discovered.
2. J. Voelcker, Tesla Model S fire in Norway caused by short circuit in car. 2016; https://www.greencarreports.com/news/1102962_tesla-model-s-fire-in-norway-caused-by-short-circuit-in-car.
3. National Transportation Safety Board, Aircraft Incident Report: Auxiliary Power Unit Battery Fire, Japan Airlines Boeing 787-8, JA829J: 2013. https://www.ntsb.gov/investigations/AccidentReports/Reports/AIR1401.pdf.
4. R. Spotnitz and J. Franklin, *Journal of Power Sources*, **113**, 81 (2003).
5. T. M. Bandhauer, S. Garimella, and T. F. Fuller, *Journal of The Electrochemical Society*, **158**, R1 (2011).
6. Q. Wang, P. Ping, X. Zhao, G. Chu, J. Sun, and C. Chen, *Journal of Power Sources*, **208**, 210 (2012).
7. R. J. Brodd, *Batteries for Sustainability*, Springer New York: New York, NY, 2013.
8. V. Ruiz, A. Pfrang, A. Kriston, N. Omar, P. van den Bossche, and L. Boon-Brett, *Renewable and Sustainable Energy Reviews*, **81**, 1427 (2018).
9. K. Kitoh and H. Nemoto, *Journal of Power Sources*, **81–82**, 887 (1999).
10. M.-S. Wu, P.-C. J. Chiang, J.-C. Lin, and Y.-S. Jan, *Electrochimica Acta*, **49**, 1803 (2004).
11. F. Larsson and B.-E. Mellander, *Journal of the Electrochemical Society*, **161**, A1611 (2014).
12. Z. Chen, R. Xiong, J. Tian, X. Shang, and J. Lu, *Applied Energy*, **184**, 365 (2016).
13. R. Zhao, J. Liu, and J. Gu, *Applied Energy*, **173**, 29 (2016).
14. A. Kriston, A. Pfrang, H. Döring, B. Fritsch, V. Ruiz, I. Adanouj, T. Kosmidou, J. Ungeheuer, and L. Boon-Brett, *Journal of Power Sources*, **361**, 170 (2017).
15. H. Maleki and J. N. Howard, *Journal of Power Sources*, **191**, 568 (2009).
16. J. Lamb and C. J. Orendorff, *Journal of Power Sources*, **247**, 189 (2014).
17. P. T. Coman, E. C. Darcy, C. T. Veje, and R. E. White, *Journal of the Electrochemical Society*, **164**, A587 (2017).
18. C. J. Orendorff, E. P. Roth, and G. Nagasubramanian, *Journal of Power Sources*, **196**, 6554 (2011).
19. M. Zhang, J. Du, L. Liu, A. Stefanopoulou, J. Siegel, L. Lu, X. He, X. Xie, and M. Ouyang, *Journal of the Electrochemical Society*, **164**, A3038 (2017).
20. D. P. Finegan, B. Tjaden, M. M. T. Heenan, R. Jervis, M. Di Michiel, A. Rack, G. Hinds, D. J. L. Brett, and P. R. Shearing, *Journal of the Electrochemical Society*, **164**, A3285 (2017).
21. B. Mao, H. Chen, Z. Cui, T. Wu, and Q. Wang, *International Journal of Heat and Mass Transfer*, **122**, 1103 (2018).
22. D. D. MacNeil, Z. Lu, Z. Chen, and J. R. Dahn, *Journal of Power Sources*, **108**, 8 (2002).
23. L. Ma, M. Nie, J. Xia, and J. R. Dahn, *Journal of Power Sources*, **327**, 145 (2016).
24. M. N. Richard, *Journal of The Electrochemical Society*, **146**, 2068 (1999).

25. S. Hildebrand, A. Rheinfeld, A. Friesen, J. Haetge, F. M. Schappacher, A. Jossen, and M. Winter, *Journal of the Electrochemical Society*, **165**, A104 (2018).
26. K. G. Gallagher, S. E. Trask, C. Bauer, T. Woehrle, S. F. Lux, M. Tschech, P. Lamp, B. J. Polzin, S. Ha, B. Long, Q. Wu, W. Lu, D. W. Dees, and A. N. Jansen, *Journal of The Electrochemical Society*, **163**, A138 (2015).
27. J.-S. Hong, *Journal of The Electrochemical Society*, **145**, 1489 (1998).
28. H. Maleki, *Journal of The Electrochemical Society*, **146**, 947 (1999).
29. W. Polifke and J. Kopitz, *Wärmeübertragung: Grundlagen, analytische und numerische Methoden*, 2nd ed.; Ing-Maschinenbau; Pearson Studium: München u.a, 2009.
30. S. Okazaki, S. Higuchi, N. Kubota, and S. Takahashi, *Journal of Applied Electrochemistry*, **16**, 631 (1986).
31. J. B. Habedank, L. Kraft, A. Rheinfeld, C. Krezdorn, A. Jossen, and M. F. Zaeh, *Journal of the Electrochemical Society*, **165**, A1563 (2018).
32. L. O. Valøen and J. N. Reimers, *Journal of The Electrochemical Society*, **152**, A882 (2005).
33. H. Lundgren, M. Behm, and G. Lindbergh, *Journal of the Electrochemical Society*, **162**, A413 (2014).
34. J. Mao, W. Tiedemann, and J. Newman, *Journal of Power Sources*, **271**, 444 (2014).
35. K. R. Crompton and B. J. Landi, *Energy & Environmental Science*, **9**, 2219 (2016).
36. R. Guo, L. Lu, M. Ouyang, and X. Feng, *Scientific Reports*, **6**, 30248 (2016).
37. C. R. Birkl, M. R. Roberts, E. McTurk, P. G. Bruce, and D. A. Howey, *Journal of Power Sources*, **341**, 373 (2017).
38. C. Fear, D. Juarez-Robles, J. A. Jeevarajan, and P. P. Mukherjee, *Journal of the Electrochemical Society*, **165**, A1639 (2018).
39. B. Rieger, S. V. Erhard, S. Kosch, M. Venator, A. Rheinfeld, and A. Jossen, *Journal of the Electrochemical Society*, **163**, A3099 (2016).